THE ABSOLUTE FLUX OF PROTONS AND HELIUM AT THE TOP OF THE ATMOSPHERE USING IMAX

W. MENN, M. HOF, O. REIMER,[1] AND M. SIMON

Universität Siegen, D-57068 Siegen, Germany

A. J. DAVIS, A. W. LABRADOR,[2] R. A. MEWALDT, AND S. M. SCHINDLER

California Institute of Technology, Pasadena, CA 91125

L. M. BARBIER, E. R. CHRISTIAN, K. E. KROMBEL, J. F. KRIZMANIC, J. W. MITCHELL,
J. F. ORMES, AND R. E. STREITMATTER

NASA Goddard Space Flight Center, Greenbelt, MD 20771

R. L. GOLDEN,[3] S. J. STOCHAJ, AND W. R. WEBBER

New Mexico State University, Las Cruces, NM 88003

AND

I. L. RASMUSSEN

Danish Space Research Institute, DK-2100 Copenhagen, Denmark

Received 1999 July 1; accepted 1999 November 23

ABSTRACT

The cosmic-ray proton and helium spectra from 0.2 GeV nucleon^{-1} to about 200 GeV nucleon^{-1} have been measured with the balloon-borne experiment Isotope Matter-Antimatter Experiment (IMAX) launched from Lynn Lake, Manitoba, Canada, in 1992. IMAX was designed to search for antiprotons and light isotopes using a superconducting magnet spectrometer together with scintillators, a time-of-flight system, and Cherenkov detectors. Using redundant detectors, an extensive examination of the instrument efficiency was carried out. We present here the absolute spectra of protons and helium corrected to the top of the atmosphere and to interstellar space. If demodulated with a solar modulation parameter of $\phi = 750$ MV, the measured interstellar spectra between 20 and 200 GV can be represented by a power law in rigidity, with $(1.42 \pm 0.21) \times 10^4 R^{-2.71 \pm 0.04}$ (m^2 GV s sr)$^{-1}$ for protons and $(3.15 \pm 1.03) \times 10^3 R^{-2.79 \pm 0.08}$ (m^2 GV s sr)$^{-1}$ for helium.

Subject headings: cosmic rays — elementary particles — ISM: abundances

1. INTRODUCTION

Protons and helium nuclei are the most abundant species in the cosmic radiation, and knowledge of their absolute abundances and the exact shape of their energy spectra is of particular astrophysical importance. Their spectral shapes are sensitive indicators of the processes of particle acceleration (Gaisser 1990), and their fluxes are the primary measure of the energy density of cosmic rays in the interstellar medium. Their spectra also serve as important inputs to calculations which aim to predict the γ-ray flux in the interstellar medium due to π^0 decay or the secondary interstellar antiproton or positron fluxes, all results of high-energy interactions of protons and helium nuclei with the interstellar gas (Gaisser 1990). Despite the importance of these most abundant cosmic-ray species, neither their absolute fluxes nor their exact spectral shape are known to adequate precision. Even at energies below 100 GeV nucleon^{-1}, where several direct measurements with balloon-borne instruments have been reported, published data on the fluxes of these particles show significant uncertainties in their absolute values and shapes. A collection of published proton spectra is given in Gaisser & Schaefer (1992), clearly illustrating the range of variation among published data. The measurement by Webber et al. (1987) at

the upper edge of this range and the measurement of Seo et al. (1992) at the lower edge differ by almost a factor of 2 in their absolute fluxes despite using essentially the same magnetic spectrometer. This shows the enormous experimental difficulty in determining absolute fluxes.

The principal problem is obtaining the efficiencies with which the detectors responded to penetrating particles during the measurement. Researchers use different methods to derive this experimental response function. Monte Carlo simulations or calibrations in the laboratory prior to flight are not ideal since experimental conditions in the gondola such as temperature or pressure may not be stable during the flight. If the response function is based on the analysis of individual detectors, systematic uncertainties are likely to introduce a bias. The best experimental determination of the instrument response function makes use of redundant detectors so that one of the detectors can be used to select a set of "good" events independent of the other detector (or detectors). These sets of events can be used to determine the efficiency of the detectors which were not involved in the selection. The Isotope Matter-Antimatter Experiment (IMAX) incorporates just such detector redundancy. IMAX uses the same superconducting magnet coil which Webber et al. (1987) and Seo et al. (1992) used in their earlier measurements. However, for IMAX the magnet was combined with new detectors which improved the overall experimental performance. This instrument is described in detail in the next section (see also Mitchell et al. 1993a).

IMAX was flown in 1992 from Lynn Lake, Manitoba, Canada, for 16 hr at an altitude of ~ 36 km. Results of this

---

flight on Galactic antiprotons (Mitchell et al. 1996) and the helium isotopes (Reimer et al. 1998) have already been published. In this paper, we present results on the absolute proton and helium fluxes in the energy range between 250 MeV nucleon^{-1} and ~ 200 GeV nucleon^{-1}. We compare these results extrapolated to the top of the atmosphere with those published earlier. In order to obtain interstellar spectra, the measured spectra were demodulated using a force field approximation (Axford & Gleeson 1968).

2. BASIC INSTRUMENT DESCRIPTION

The IMAX experiment (Fig. 1) was designed to measure cosmic-ray antiprotons, the abundances of light isotopes, and cosmic-ray spectra (Mitchell et al. 1993a). Particle identification in IMAX is based on the determination of the charge (Z), velocity (β), and magnetic rigidity (R) of incident particles using a high-resolution time-of-flight (TOF) system, large-area silica aerogel and polytetrafluorethylene (PTFE) Cherenkov detectors, high-precision drift chambers (DCs), and high-resolution scintillation counters. IMAX used the NASA/NMSU Balloon-Borne Magnet Facility (BBMF) payload (Golden et al. 1978), including the superconducting magnet and multiwire proportional chambers (MWPCs).

The rigidity (momentum/charge) of an incident particle is measured by determining its trajectory in the field of a 61 cm diameter single-coil superconducting magnet, which
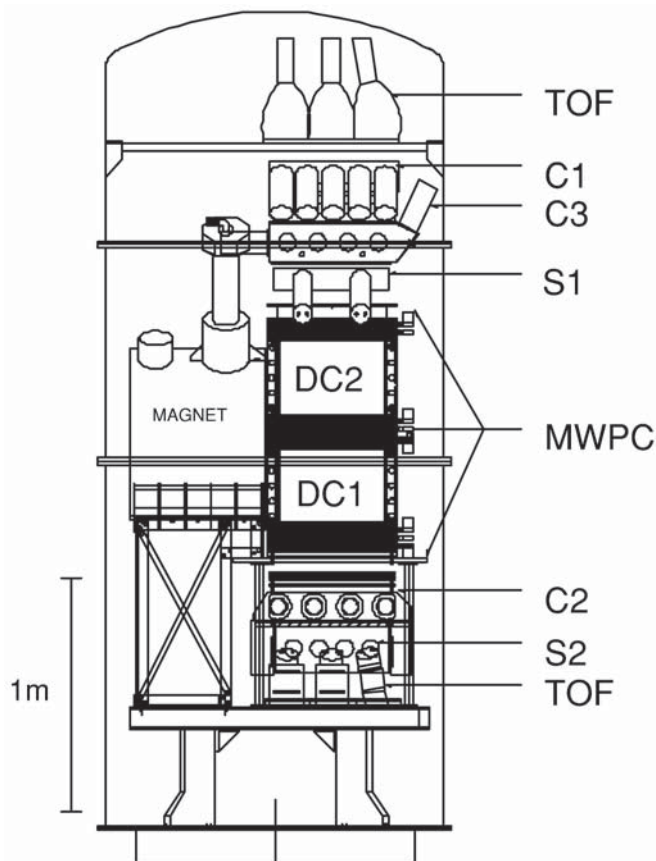

FIG. 1.—IMAX instrument. TOF is the time-of-flight system, and C1 is a PTFE Cherenkov detector. C2 and C3 are the silica aerogel Cherenkov detectors, S1 and S2 are light-integrating plastic scintillators, MWPCs are the three separate sets of multiwire proportional chambers, and DC1 and DC2 are the DC modules.

varies from 0.1 to 2.1 T in the region of the tracking detectors. The tracking system is a combination of DCs and MWPCs. Both systems can be analyzed independently. For the isotope and antiproton measurements the two systems are combined to get the highest momentum resolution (Mitchell et al. 1996; Reimer et al. 1998). However, for the spectrum analysis described here, the trajectories were calculated using the DC alone and the MWPCs were used for efficiency determination.

The DC system consists of two identical DC modules, each with an inner gas volume of $47 \times 47 \times 35$ cm^3 (Hof et al. 1994). Each chamber contains six measurement layers for the X (bending)-coordinate and four layers for the Y (nonbending)-coordinate. Each layer contains 16 hexagonal drift cells with a radius of 15.6 mm in a close-packed structure. Pure CO_2 was used as a drift gas because its drift velocity is very slow and the effects of the magnetic field (Lorentz forces) on the liberated drift electrons are small. This greatly reduces the sensitivity of the time path relationship of the drift electrons to the inhomogenous field. For singly charged particles the anode wires are normally operated at 4600 V. In the IMAX flight the high voltage was set to 4450 V to reduce the charge amplification at the sense wire and to optimize the spatial resolution for helium nuclei. This has only a minor effect on the spatial resolution for protons and slightly reduces the efficiency with which they are detected (see § 4.4). The 320 anode wires were read out using a LeCroy 4290 time-to-digital converter (TDC) system (3 ns count^{-1}) via LeCroy 2735 DC preamp/discriminator cards with leading-edge discrimination at a fixed, but adjustable threshold. For more details, see Hof et al. (1994).

In addition to the DCs, IMAX has a system of MWPCs with an area of 48×48 cm^2. The MWPC system consists of eight X-coordinate layers and four Y-coordinate layers, with three X-coordinate layers (two Y-coordinate layers) below the bottom DC, three X-coordinate layers (two Y-coordinate layers) between the DCs, and two X-coordinate layers (one Y-coordinate layer) above the top DC. The track position measurement for each coordinate axis was obtained measuring the arrival time of the signal at each end of delay lines using custom constant-fraction discriminators and LeCroy 4208 TDCs. The chambers are operated with "magic gas" (a mixture of argon, isobutane, and freon). The MWPCs are described in detail in Golden et al. (1991).

The particle track is obtained from a mathematical procedure which is based on the integration of the equation of motion in the (known) magnetic field for a set of five free parameters: the deflection η (the inverse of the rigidity), the two direction cosines, and the (X, Y)-position of the track in the first DC layer. Each trajectory is fully defined by these five parameters. In an iterative procedure the final values for the parameters are obtained by minimizing the deviations between the position measurements made by the track detectors and the computed trajectory. The algorithm also provides the uncertainties in the five parameters. Details of the fitting procedure can be found in Golden et al. (1991).

To use the DC, a time-to-space function which converts the measured drift times to drift paths must be derived. This procedure is described in detail in Hof et al. (1994). Applying corrections for the geometry of the layers and the reduced degrees of freedom of the fit, we used the deviations

between the measurements and the computed trajectories to obtain the spatial resolution of the chamber. The average resolution at the high voltage used for the IMAX flight is around 90 μm for protons and 65 μm for helium, reaching 70 μm for protons and 50 μm for helium for medium-drift distances. The X- and Y-coordinate layers have the same resolution.

The MWPC requires the measured times at the ends of the delay lines to be converted to positions. To first order this is a linear function, but because of small variations in the signal velocity nonlinear terms must be added. For details of the procedure see Golden et al. (1991). The resolution for the X-coordinate layers varied between 250 and 1000 μm, whereas the resolution for all Y-coordinate layers was about 1000 μm. There was no significant difference in position resolution between $Z = 1$ and $Z = 2$ particles.

The particle velocities are obtained in two regimes using different measurement techniques. For energies up to 2 GeV nucleon^{-1}, a high-resolution time-of-flight system is used (Mitchell et al. 1993b). The system consists of two planes of Bicron BC-420 plastic scintillator 2.54 m apart, each made up of three $60 \times 20 \times 1$ cm^3 scintillators. Hamamatsu R 2083 photomultiplier tubes (PMTs) are coupled to the end of the paddles by adiabatic light pipes. Each PMT anode signal is split differentially and sent to a LeCroy 2249A analog-to-digital converter (ADC) and a LeCroy 4413 leading-edge discriminator with the threshold set to 15 mV. The pulses for minimum ionizing particles are generally above 100 mV so detection efficiency is very high. The arrival times of the discriminator pulses are digitized using LeCroy 2229 TDCs Mod 400 (channel width 30 ps). The overall timing resolution of the TOF system is 122 ps for $Z = 1$ and $\beta = 1$ particles and 92 ps for relativistic helium (Mitchell et al. 1996; Reimer et al. 1998).

For antiproton and isotope measurements in the energy range from 2.5 to 3.7 GeV nucleon^{-1}, velocities are measured by two large-area silica aerogel Cherenkov detectors (C2 and C3). However, they are not used for the spectrum analysis, nor is a third Cherenkov detector (C1) with a PTFE radiator used.

The charge of an incident particle is derived from four independent ionization energy loss measurements using the two TOF layers and two large-area light-integrating scintillation counters (S1 and S2). S1 contains a $51 \times 51 \times 1$ cm^3 Bicron BC 400 plastic scintillator, viewed by four 3″ Hamamatsu R 1307 PMTs. The four PMT signals are combined into two pairs which are pulse-height analyzed with LeCroy 2249A ADCs. S2 contains a $55 \times 49 \times 1.8$ cm^3 Bicron BC-408 plastic scintillator, viewed by 12 2″ Hamamatsu R2409-01 PMTs. All phototubes are individually pulse-height analyzed with LeCroy 2249A ADCs. Charge is determined using a dE/dx versus β^2 method (a dE/dx vs. η^2 method is also possible). The capability of this method is illustrated in Figure 2, which shows the excellent charge separation obtained from the S2 scintillator. In Figure 2 the solid lines define bands which are used to select the charge. By combining multiple independent energy loss measurements, IMAX obtains a very high certainty in charge identification. In addition, the detection efficiencies can be accurately determined via cross checks between scintillators.

The normal IMAX event trigger was a fourfold coincidence of PMT signals from the two TOF layers, requiring
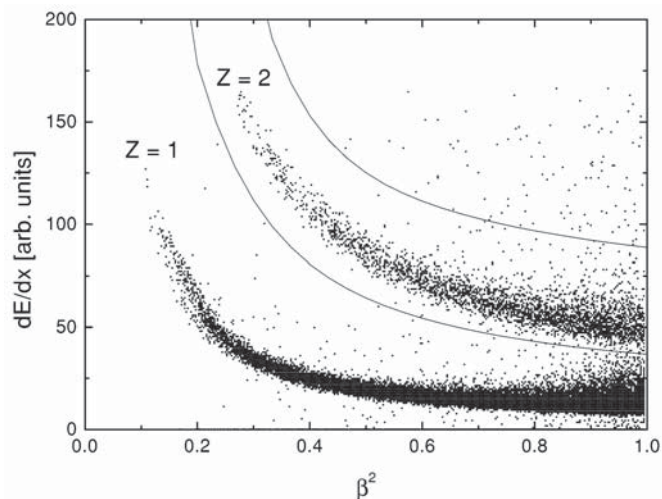

FIG. 2.—Charge separation obtained with the S2 scintillator, illustrated by plotting the ionization energy loss vs. the squared particle velocity. The solid curves show the chosen charge regions.

two PMTs from opposite sides of the top layer and two from opposite sides of the bottom layer. The coincidence level could be reprogrammed in flight.

3. FLIGHT

IMAX was launched from Lynn Lake, Manitoba, Canada (56°.5 north latitude, 101° west longitude), on 1992 July 16. Float duration was 16 hr at an average altitude of 36 km with an atmospheric overburden of about 5 g cm^{-2}. At the end of the float period, the magnet was ramped down and data were taken with the magnet off in order to check the alignment of the tracking chambers. Landing was near Peace River, Alberta, Canada (56°.6 north latitude, 118° west longitude), with the instrument recovered in excellent condition. Over 3.6×10^6 events were recorded during the float period. The geomagnetic cutoff increased from 0.37 GV at Lynn Lake to 0.63 GV at Peace River (using cutoff tables from Shea & Smart 1983).

4. DATA ANALYSIS

4.1. Fundamental Data Analysis and Selection Criteria

During the 16 hr of float the on-board computer registered 3.6×10^6 events. The data used for this analysis were recovered from analog tapes, and one tape (~ 30 minutes of float data) was not usable. Comparing the event numbers from the usable tapes with the numbers from the on-board computers it was found that about 6% of the data were lost as a result of telemetry and recording errors. Each frame of the raw data was also checked for consistency with a checksum. Finally 3.3×10^6 events of the data proved usable. The next step in the analysis was trying to fit a track for each event, with an iterative fitting procedure requiring a minimum of four measurements in the X-coordinate and three in the Y-coordinate. Using the information from all hit drift cells, the algorithm fits only one "best" track. The most important criterion for track selection is the number of measurements used in the fit. If more than one track is found with the same number of measurements, the track with the lowest χ^2 is selected. The danger of missing a good event by this procedure is on the order of 1% and will be considered in § 4.4. With this procedure we fit 1.6×10^6 events successfully. This drastic reduction in the number of

accepted events results from the background caused by showers in the instrument, in the magnet, and in the residual atmosphere. These showers exhibit either multiple tracks or a low number of hits in the DC, usually resulting in a failed fitting procedure (see also Smith et al. 1973). Note that the fitted 1.6×10^6 events will still contain some multiple-track events for which a track could be obtained.

To the events remaining after the track-fitting procedure we applied the following requirements (see Table 1 for further details):

1. The track must pass through the sensitive volume of all detectors.

2. Only one paddle hit is allowed in the top and bottom TOF scintillators.

3. Threefold charge selection is used with the top and bottom TOF scintillators and S2 (S1 is only used for cross checks).

4. Tracking quality cuts:

a) The number of DC layers with hits more than 4 cm outside the fitted track must be less than three for each coordinate; a multiple-particle event will show DC hits outside the fitted track and should be rejected; however, electronic cross talk may result in signals in the channels adjacent to the hit drift cell; to save these events, a distance of 4 cm (1.5 drift cell diameter) is used.

b) A minimum of nine (out of 12) measurements in the X-coordinate (N_x) and six (out of eight) in the Y-coordinate (N_y) must be used in the fit.

c) χ^2 for each coordinate must be less than 4.

The rigidities of events with a positive charge which pass these cuts are to first order the rigidity spectra for particles with charge $Z = 1$ and $Z = 2$. We derive the energy spectra (particles GeV^{-1} nucleon^{-1}) by considering all $Z = 1$ particles to be protons and all $Z = 2$ particles to be ^{4}He. Although this simplification is a common procedure used by other authors, it is clear that this will lead to an error in the spectra since there is a background of other particles (muons, deuterium) in the $Z = 1$ data sample and even a significant fraction of ^{3}He in the helium data. We discuss corrections for the $Z = 1$ background below. For comparison with other authors, we do not correct the helium spectrum for the ^{3}He. However, in the Appendix we describe an improved calculation where we take the isotopic ratio measured by IMAX into account.

4.2. Correction for $Z = 1$ Background

The $Z = 1$ data sample consists of protons, deuterium, tritium, and the light particles like muons, pions, kaons, and positrons. To get the pure proton spectrum, one has to subtract this background. We could use the particle identification capability of the magnetic spectrometer in combination with the TOF and Cherenkov detectors for background rejection, but above ~ 3.5 GeV nucleon^{-1} the proton sample would still be contaminated because the instrument cannot distinguish the protons from the background (Reimer et al. 1995).

To get the unknown spectrum of the positively charged light particles, we first derived the spectrum of the negatively charged light particles by selecting all events with negative rigidity. This sample contains negative muons, pions, kaons, electrons, and a negligible fraction of antiprotons. The ratio of positively to negatively charged light particles can be derived from the IMAX data using the TOF, which allows a good separation between positively charged light particles and protons at low rigidities ($R < 2$ GV). Assuming that this ratio, which was found to be about 1.25, does not depend on rigidity, we multiply the measured negative spectrum by this ratio to obtain the spectrum of the light positively charged particles. At low rigidities they make a significant contribution of about 10% to the overall $Z = 1$ spectrum, but at higher rigidities the fraction drops well below 1%.

The amount of deuterium contamination was determined using the particle identification capability of the IMAX instrument in an energy regime below ~ 3 GeV nucleon^{-1} to derive the ^{2}H/^{1}H ratio, although we will have no information for higher energies. The result is presented by Reimer et al. (1995) using information from the TOF and the aerogel Cherenkov detectors. In that paper, the ^{2}H/^{1}H ratio at the instrument is given as a function of energy per nucleon, decreasing rapidly from about 6.5% at 300 MeV nucleon^{-1} to less than 2% at 2.8 GeV nucleon^{-1}. Above 3 GeV nucleon^{-1}, we set the ^{2}H/^{1}H ratio to be constant at 1.5%. Converting this ratio to a function of rigidity, the ^{2}H/^{1}H ratio is small ($<1\%$) at low rigidities and increases to $\sim 5\%$ for higher rigidities. At balloon flight altitudes there is also a small amount of locally produced ^{3}H in the $Z = 1$ background. From the IMAX data we determined directly that this is only a small fraction of the deuterium abundance (Reimer et al. 1995) and therefore ignore this background contribution.

TABLE 1
SELECTION CRITERIA STATISTICS FOR THE IMAX DATA USED
FOR THE SPECTRUM ANALYSIS

	INDIVIDUAL CUT		RUNNING FRACTION	
SELECTION CRITERION	Events	Percentage	Events	Percentage
Fit okay....................	1,641,972	100	1,641,972	100
$R > 0$.....................	1,516,676	92.4	1,516,676	92.4
Fit inside geometry	1,159,225	70.6	1,102,183	67.1
Single paddle hit	1,410,452	85.9	1,005,576	61.2
No multihit in DC........	1,484,381	90.4	962,189	58.6
$NG_x \geq 9$, $NG_y \geq 6$......	916,368	55.8	614,993	37.5
$\chi^2_{x,y} < 4$....................	1,147,046	69.9	492,680	30.0
Charge agreement	1,501,910	91.5	464,376	28.3
$Z = 1$	1,430,686	87.1	429,039	26.2
$Z = 2$	71,224	4.3	35,337	2.2

4.3. *Influence of the Spectrometer Precision*

While the contamination by light particles and deuterium is the greatest source of uncertainty in the proton spectrum at low energies, the measured spectra at high energies are distorted as a result of the limited spectrometer precision. The rigidity resolution of the magnet spectrometer is limited by the spatial resolution σ of the position measurements, the number of measurements N, and the magnetic field strength ($\int Bdl$) in the volume which the particles traverse. The relative error in determining the rigidity can be approximated (Gluckstern 1963) as

$$\frac{\Delta R}{R} \sim \frac{R\sigma}{\int Bdl}\frac{1}{\sqrt{N+4}}$$

or with

$$\eta = 1/R, \quad \Delta\eta \sim \frac{\sigma}{\int Bdl}\frac{1}{\sqrt{N+4}}. \tag{1}$$

In the IMAX analysis the error in the deflection measurement $\Delta\eta$ is obtained for each event mathematically from the fitting algorithm. In Figure 3 the $\Delta\eta$ distribution for protons and helium is shown. In IMAX the magnetic field is inhomogenous and $\int Bdl$ varies for each event since the particles penetrate different regions of the sensitive volume. This results in a distribution with a tail toward high $\Delta\eta$. The $\Delta\eta$ distribution for helium is shifted to the left because the spatial resolution for helium is better than for protons. It is common to define a maximum detectable rigidity (MDR) as the rigidity for which the measurement error is 100% ($\Delta R/R = 1$). We use the peak of the $\Delta\eta$ distribution, the most probable deflection error, to obtain a single number for the MDR. This leads to an MDR of 175 GV for protons and an MDR of 250 GV for helium using only the DC system.

The spectrometer resolution function can be defined as the distribution of measured deflections for tracks whose actual curvature is zero (straight tracks). If $\Delta\eta$ were constant, the resolution function would be a simple Gaussian. But since $\Delta\eta$ follows the distribution shown in Figure 3, the resolution function is more complex. We generate this func-

tion by performing a convolution of Gaussians with widths distributed as in Figure 3. The resolution functions for protons and helium obtained by this method are shown in Figure 4. The narrow peak results because most of the measurements have small $\Delta\eta$ values, and the tails are due a small fraction of events with large $\Delta\eta$. In principle, this resolution function can also be obtained from a direct measurement of straight tracks with the magnet off. The measured tracks are analyzed as if they were high-rigidity events with the magnet on. The resulting deflection distribution is the resolution function. The preselection of high-energy particles with an independent detector is necessary to avoid effects due to multiple scattering, which would widen the measured resolution function. Unfortunately, in the IMAX instrument we had no effective means to preselect high-energy particles. Thus, we derive the resolution function shown in Figure 4 by the mathematical procedure described above. However, the experimental approach was tested successfully in the MASS2 experiment (M. Hof 1997, private communication). The MASS2 experiment uses the same magnetic spectrometer as IMAX but allows a selection of high-energy particles with a gas Cherenkov counter ($\gamma > 20$). For further discussion of this topic see Reimer et al. (1998).

Now we consider in detail how the limited spectrometer resolution affects the measured spectrum. With decreasing deflection the relative error in the deflection measurement increases, which makes it impossible to resolve details in the spectrum since adjacent bins are correlated. Also, it becomes more and more likely that high-energy positively charged particles may be assigned the wrong bending direction ("spillover"). This is clearly seen in Figure 5, where we show the measured deflection spectrum for protons. The loss of positively charged particles leads to a distortion of the spectrum, and the measured rigidity (or energy) spectrum will be steepened. To correct the spectrum for this effect, it has to be "deconvolved" using the measured deflection spectrum and the resolution function of the instrument. One approach is to use a Monte Carlo, which incorporates the resolution function and an assumed incident spectrum to generate simulated data. The difference between the simulated data and the input spectrum as a
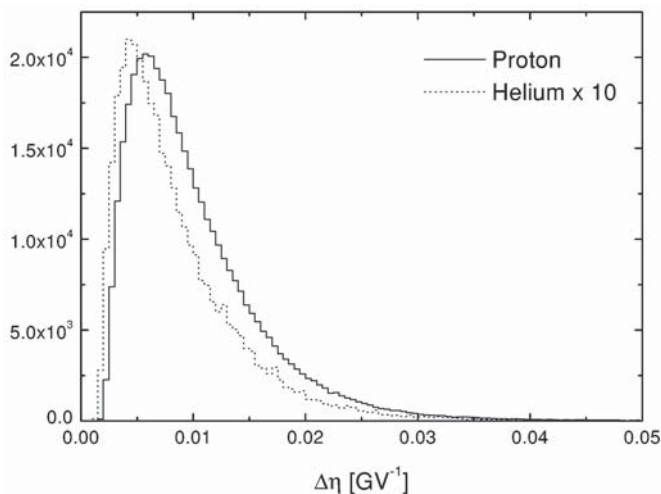

FIG. 3.—Distribution of the deflection resolution for protons and helium. Note that the distribution for protons peaks at 0.0057 GV^{-1}, corresponding to an MDR of 175 GV, while the peak for helium is at 0.004 GV^{-1} (MDR = 250 GV).
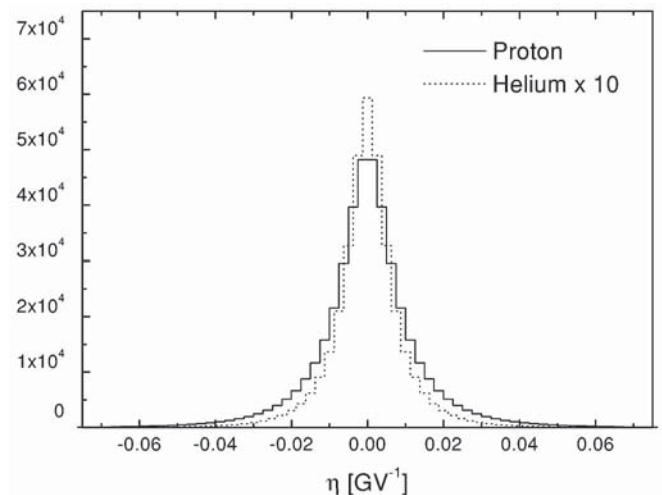

FIG. 4.—Simulated resolution function of the magnetic spectrometer for protons and helium obtained by performing a convolution of Gaussians having the width distribution given in Fig. 3.
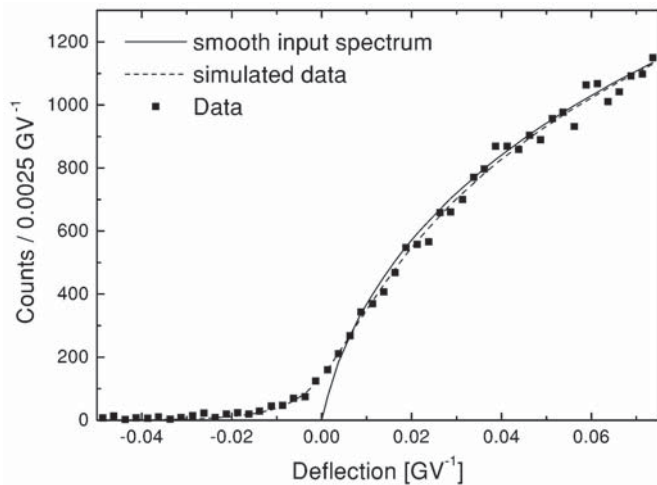
FIG. 5.—Deconvolution of the deflection spectrum for protons to account for finite spectrometer resolution. The simulated data curve (*dashed line*) is the result of a convolution of a smooth input spectrum (*solid line*) with the resolution function.

FIG. 6.—"Deconvolution factor" for protons derived using the described deconvolution procedure. The three curves refer to different numbers of free parameters for the assumed input spectrum.

function of rigidity is then used for the deconvolution. Another method is to calculate the unknown incoming spectrum in an iterative way by convolving a deflection histogram of the assumed incoming spectrum with the resolution function, thus getting a simulated data histogram which is then compared with the measurement. By varying the bins in the histogram of the incoming spectrum, the best match between simulation and data is found. However, in attempting to apply this technique to the IMAX analysis, statistical fluctuations in the observed spectrum caused unphysical oscillations in the derived incoming spectrum. This was also observed in other experiments (Seo et al. 1992). We therefore applied a different method, an iterative procedure in which we started with an assumed smooth incident spectrum. We describe this incident spectrum by a third-order polynomial in a log (flux) versus log (R) representation with four free parameters:

$$\log (\text{flux}) = A + B \log (R) + C[\log (R)]^2 + D[\log (R)]^3 .$$

(2)

We start with a guess for the four parameters A, B, C, and D and then transform the rigidity spectrum into a deflection spectrum and convolve it with the IMAX resolution function. This procedure mimics the IMAX instrument, and we compare the simulated result with the measured IMAX deflection spectrum by means of a χ^2 analysis, with χ^2 defined as

$$\chi^2 = \sum_{i=1}^{\text{max bin}} \frac{(N_i - n_i)^2}{\sigma_i^2} , \quad \text{with } \sigma_i^2 = \sqrt{n_i} ,$$

(3)

where N_i is the number of events in the ith bin of the simulation and n_i is the number of events in the ith bin of the data histogram. Varying the four parameters we minimize χ^2 to find the best smooth input spectrum, which is shown for the protons in Figure 5. The dashed line represents the simulated IMAX response. This curve describes the spillover at high rigidities (low deflections) very well. The ratio of the solid line (smooth input spectrum) to the dashed line (simulated spectrum) as a function of rigidity gives the
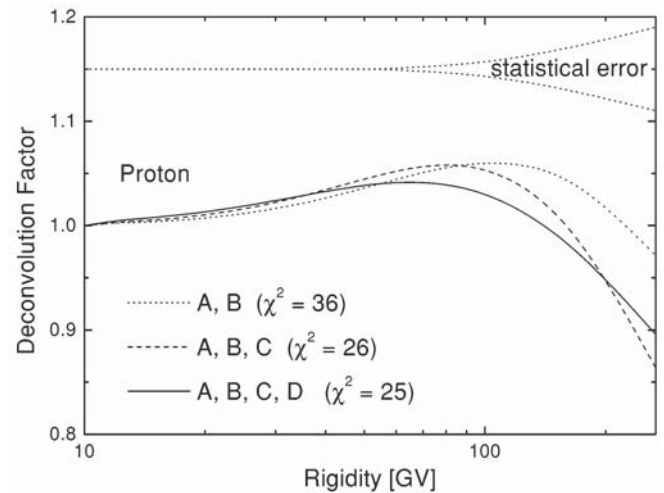
amount of correction to the data required to account for the spillover. This ratio is shown for protons in Figure 6. The three different curves refer to different shapes (different number of free parameters in eq. [1]) of the assumed input spectrum in our simulation. The solid curve results when we use a third-order polynomial as the assumed input spectrum, the dashed curve follows from a second-order polynomial, and the dotted curve follows when we assume that the input spectrum is a pure power law. The statistical uncertainties, which are inherent in the data at different rigidities, are plotted at the top of Figure 6. The correction which we have to apply to the measured deflection spectrum is close to one at low rigidities, independent of the assumed input spectrum. At high rigidities the spillover correction becomes more and more pronounced and the actual value is relatively insensitive to the assumed input spectrum in the simulation procedure, at least within statistical uncertainties. Note that because of the high quality of the spectrometer, the distortion of the measured spectrum up to about 200 GV is smaller than 5%. In our analysis we used the correction given by the solid curve (third-order polynomial as the input spectrum) since it is mathematically more sensitive and provides the best fit to the data with the smallest χ^2 value (see Fig. 6). In the next step of the analysis we multiply the measured rigidity spectrum by the derived deconvolution factor.

4.4. *Corrections Due to Detector Efficiencies*

To obtain absolute fluxes of cosmic-ray particles from a complex instrument is a very complicated task experimentally since it requires that the efficiencies of all detectors under the conditions of the applied cuts are fully understood. It is impossible to derive the efficiency of a detector using only its own measurements without potentially introducing a bias. The cleanest experimental approach is to use an independent detector B of the instrument to select single particles passing through detector A. The response or the efficiency of detector A can then be studied directly. The IMAX instrument has such an experimental configuration. The tracking system consists of the two independent devices, the DC and the MWPC, so it is possible to test the

DC by using the MWPC to select events. Similarly, the charge is measured with four independent scintillators. In order to obtain the charge detection efficiency for one of the four scintillators, we preselect events with a threefold charge consistency of the remaining detectors and determine the response in the scintillator of interest.

In the final analysis of the IMAX data we determine the charge by a threefold charge consistency between the upper and lower TOF scintillators and the S2 scintillator. In Figure 7 we present the charge detection efficiency for this combination for protons and helium as a function of energy. In these response curves there is a weak energy dependence, and the detection efficiency for helium is below that for protons. We do not attribute this to a physical process since the actual separation of protons and helium nuclei depends on the bands in Figure 2, which are chosen somewhat arbitrarily. Thus, in addition to the statistical error in these detection efficiencies we apply a systematic error of $\pm 1\%$ to account for the selection process.

Determining the detection efficiency of the DC is more complex, but the approach is similar. We want to determine the DC efficiency for single tracks and noninteracting particles which penetrate the instrument. In order to preselect such a sample of events we use the whole instrument except the DC. The following selection criteria have to be fulfilled: (a) successful track-fitting using the MWPC alone; (b) the track passing the DC volume, the top and bottom TOF, and S2; (c) only single paddle hits in the top and bottom TOF; (d) charge consistency among the top and bottom TOF and S2; and (e) if charge $Z = 1$ is detected, the selection of protons using the TOF. (This is possible only below ~ 2 GeV nucleon^{-1}. At higher rigidities we have contamination on the order of a few percent from light particles; see § 4.2.) These criteria should not be confused with the actual data cuts which we presented in § 4.1 and which are used for the IMAX spectrum analysis. The selection criteria here only give confidence that uninteracted particles which penetrate the DC are selected for the DC efficiency determination.

The response of the DC to these particles is checked, applying different cuts to the DC fits, and we show the result in Figure 8. The upper two curves are obtained when
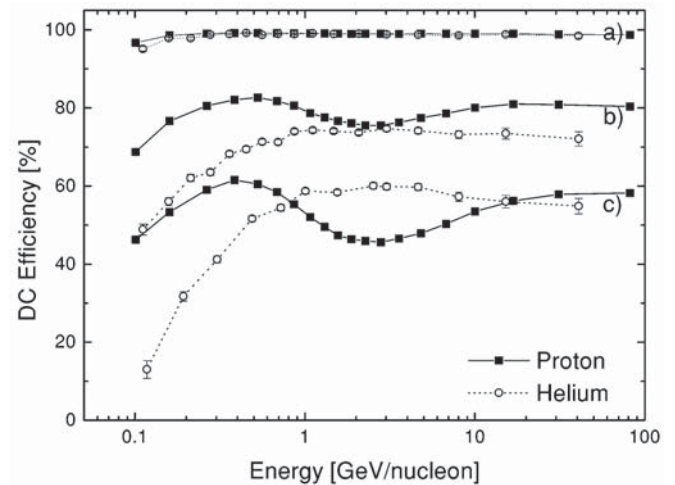
FIG. 8.—Detection efficiency of the DC for protons and helium. Curve *a* corresponds to minimum tracking quality requirements (*X*-coordinate measurements, $N_x \geq 4$; *Y*-coordinate measurements, $N_y \geq 3$), curve *c* corresponds to the quality cuts used for the spectrum analysis ($N_x \geq 9$, $N_y \geq 6$, $\chi^2 < 4$), and curve *b* corresponds to an intermediate requirement ($N_x \geq 7$, $N_y \geq 5$, $\chi^2 < 8$).

we require only a minimum quality of the DC track fit: a converged fitting procedure and at least four measurements in the *X*-coordinate and three in the *Y*-coordinate. These are the same requirements we used in the analysis of the raw data in § 4.1. Under these loose conditions we find the efficiency to be almost constant at around 99% for protons and 98% for helium with a slight decrease at low energies. The lower two curves result when we apply the cuts that we use for the IMAX data analysis, listed in § 4.1. The two curves in the middle correspond to an intermediate condition. As a general trend, the stronger the requirements on the DC tracks, the smaller the efficiency becomes and more energy dependence appears.

While it is obvious that stronger constraints on the fitting conditions will reduce the overall detection efficiency, the interpretation of the energy dependence is more interesting and needs a closer look. The decrease in the efficiency at low energies we attribute to a combination of multiple scattering and the applied χ^2 cut and to the track-fitting algorithm. Multiple scattering which affects the low-energy particles causes a large deviation between the measurements of the track detector and the fitted track, which we could observe in the data (Hof et al. 1994). As a consequence, the χ^2 values for a low-velocity track are increased. By applying a χ^2 cut, the low-energy particles are preferentially removed. The reason that the efficiency for helium at low energies is below that of the protons is the higher ionization density along their tracks and the subsequent charge multiplication at the sense wires. This leads to an increase in cross talk to adjacent drift cells and preamplifiers and some of these events are eliminated by the data cuts. For protons, there is an additional dip in the efficiency curve around 2 GeV. To examine this behavior, we determined the efficiency of a single drift cell for protons and helium as a function of energy for the reference data sample. We show the results in Figure 9. While the average drift cell efficiency for helium is $\sim 98\%$, it is only $\sim 93\%$ for protons. This is caused by our choice of the high voltage of the anode wires (see § 2). The voltage was set to 4450 V to optimize the resolution for helium. This leads to a decreased
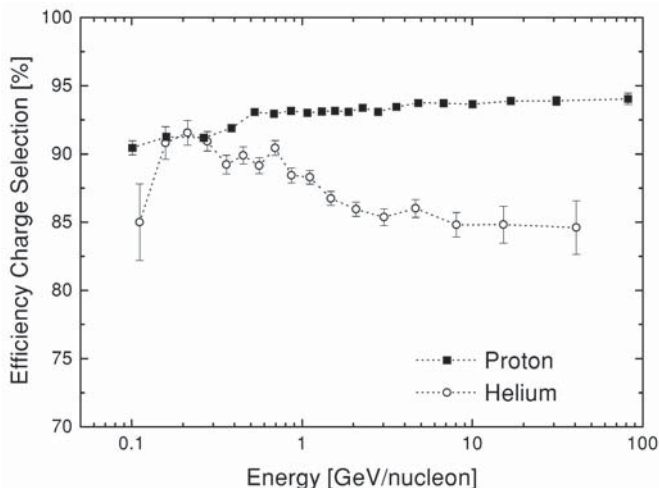

FIG. 7.—Charge selection efficiency for protons and helium for a threefold charge consistency of the top and bottom TOF and the S2 detector. The method of charge selection is shown in Fig. 2.
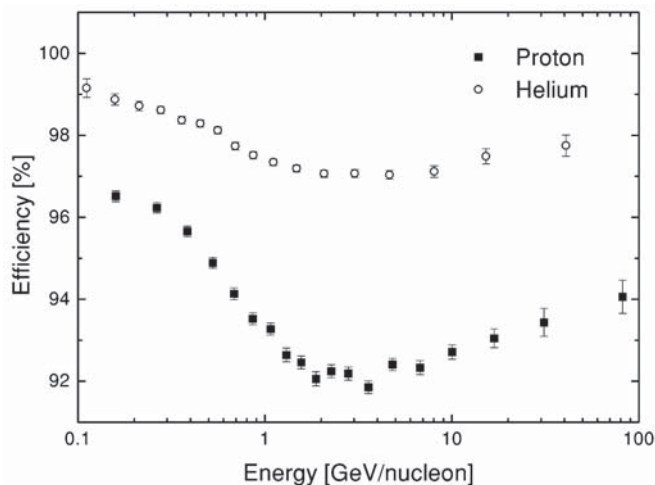
FIG. 9.—Efficiency of a single drift cell as a function of kinetic energy for protons and helium.
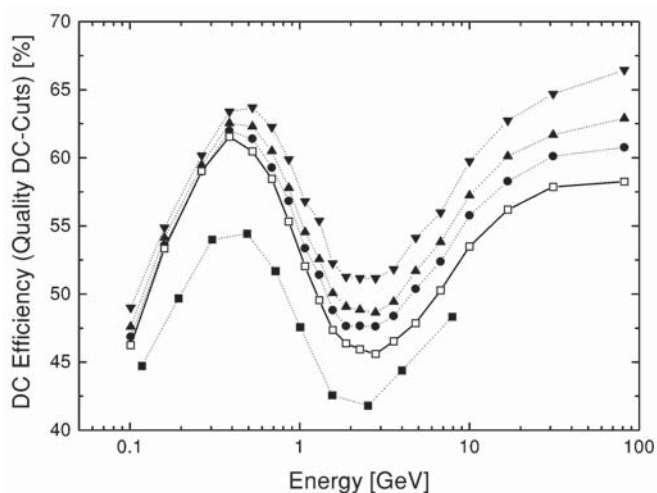

FIG. 10.—Detection efficiency of the DC for protons using the standard quality cuts described in § 4.1. The reference data sample was obtained using the MWPC (applied cuts to the MWPC; *open squares*: $N_x \geq 4$, $N_y \geq 2$; *filled circles*: $N_x \geq 5$, $N_y \geq 3$, $\chi^2 < 8$; *upright triangles*: $N_x \geq 6$, $N_y \geq 3$, $\chi^2 < 6$; *inverted triangles*: $N_x \geq 7$, $N_y \geq 3$, $\chi^2 < 4$) or the scintillators only (*filled squares*).

efficiency for single charged particles because of the lower ionization. The effect of the ionization loss as a function of the energy is also clear in Figure 9, giving a minimum at 2 GeV nucleon^{-1}, especially for the $Z = 1$ particles. This drop in the efficiency of the individual drift cells will cause protons in that energy range to be preferentially removed by our cut on the number of measurements used in the fit (see § 4.1).

Although these results give a good understanding of the DC tracking efficiencies, the possibility of hidden systematic errors due to remaining correlations between the DC and the MWPC must be considered. Interactions in the DC could influence the MWPC selection, or the types of events which fail in the MWPC and DC tracking may be correlated. Therefore, we performed an additional test. We selected events using the four scintillators (the top and bottom TOF, S1, and S2), and in the top and bottom TOF only single paddle hits were allowed. Even without tracking information the particle velocity can be derived using the position information from the TOF system to measure a flight path length. Although the β measurement obtained in this way is not as accurate as using the track information, it is good enough to select a charge in combination with the dE/dx signal in the scintillators. A fourfold coincidence of the top and bottom TOF, S1, and S2 is defined as a single track.

We also repeated our original method of event selection using the MWPC and applying stronger and stronger quality cuts to the MWPC fit. This tests whether the quality of the reference data has an effect on the DC efficiency. The results of both the MWPC and scintillator preselection of proton events are shown in Figure 10. All curves in Figure 10 were generated requiring the same fitting constraints on the DC track quality that we use in the full IMAX analysis (§ 4.1). They differ only in the quality of the MWPC preselection. The efficiency curve shown in Figure 10 by the solid line with open squares is identical to curve c of Figure 8, but with an expanded vertical scale. Note that all curves in Figure 10 are similar in shape but their absolute values differ by roughly $\pm 5\%$ with respect to the solid line. There is also a clear correlation between the DC and MWPC. With stronger preselection criteria applied to the MWPC, higher track efficiencies were obtained for the DC. We con-

sider the DC efficiency calculated under the strongest cuts on the MWPC preselection as an upper limit to the DC efficiency. Similarly, the DC efficiency obtained using only the scintillator preselection represents the lower limit. We checked many individual events which passed the scintillator criteria but failed the DC fit and found a background of events with multiple tracks from air showers which satisfy the scintillator criteria but do not have a track through the DC. From these studies we conclude that a conservative estimate of the uncertainty in the absolute DC tracking efficiency is $\pm 5\%$.

4.5. *Corrections for Interactions in the Instrument*

In the last section we dealt with the efficiencies of the various detectors which have to be understood in order to obtain the absolute flux of incoming particles. These efficiencies were derived by preselecting single, noninteracting particles. However, we must also account for incident nuclei that interact in the material of the instrument. These could fail to fulfill either our preselection cuts (§ 4.4) or final cuts (§ 4.1). Events which pass the preselection but do not pass a final detector cut are accounted for in the detector efficiencies. However, for those events which fail both the preselection *and* final cuts a correction must be calculated since we cannot derive the abundance of those events from the data. Like other authors, we correct for inelastic interactions of the particles but, in addition, we will also correct for the influence of δ-electrons (or δ-rays).

4.5.1. *Correction for Inelastic Interactions*

Inelastic interactions can lead to the production of spallation products or new particles or cause a hard scatter that can significantly alter the original direction of the incoming particle. The combination of cuts used in the IMAX spectrum analysis (§ 4.1) efficiently select against these effects, and we assume that all inelastic interactions in the instrument are eliminated. The multiple-track signature of many of these events will be identified either by the DC or by the TOF, and hard scatters will result in large χ^2 values from

the fitting algorithm. Interactions may also result in inconsistent charge measurements.

If all inelastic interactions are recognized and vetoed by the instrument, then the calculated interaction probability provides the appropriate correction factor. IMAX has a total of 16.7 g cm^{-2} from the top of the instrument to the bottom of the lower TOF and 10.7 g cm^{-2} from the top of the instrument to the bottom of the DC. A lower limit of correction for inelastic interactions is the interaction probability caused by the 10.7 g cm^{-2} of material above the bottom of the DC. However, there is a reasonable chance that interactions which occur in the material below the DC will also be vetoed by failing charge consistency or by causing multiple hits in the TOF. Thus, we assume that the calculated interaction rate in the total 16.7 g cm^{-2} provides the upper limit of correction.

The total inelastic cross section for protons on nuclei is given by

$$\sigma_{p-\delta A \geq 1} = \sigma_{p-\delta A \geq 1}(\text{he})$$
$$\times \left[1 - 0.62 \exp\left(-E/200\right) \sin\left(10.9 E^{-0.28}\right)\right], \quad (4)$$

where E is the kinetic energy of the projectile in MeV per nucleon. The energy-dependent term is taken from Letaw et al. (1983), the values for the high-energy cross section $\sigma_{p-\delta A \geq 1}(\text{he})$ are taken from Review of Particle Properties (1998).

The equation for the mass-changing cross sections for helium on nuclei is taken from Reimer et al. (1998), where the authors parameterized data from Aksinenko et al. (1980), Auce et al. (1994), DeVries et al. (1982), Dubar et al. (1989), Tanihata et al. (1985), and Webber et al. (1990a, 1990b, 1990c, 1990d) as

$$\sigma_{^4\text{He}-\delta A \geq 1} = 10\pi(1.075 A_T^{0.355} + 1.4)^2$$
$$\times \left[1 - 0.62 \exp\left(-E/200\right) \sin\left(10.9 E^{-0.28}\right)\right], \quad (5)$$

where A_T is the mass number of the target nucleus. We use the total mass-changing cross section because we assume that all measured helium is ^{4}He.

For the calculation, we take the different materials along the path of the particle into account. The inelastic interaction probability at high energies for protons is 13% for 10.7 g cm^{-2} of material and 19% for 16.7 g cm^{-2}. For helium we find a probability of 27% for 10.7 g cm^{-2} of material and 47% for 16.7 g cm^{-2}. In our analysis of the total fluxes, we adopt the mean values of these probabilities. The separation of the means from the upper and lower limits are about $\pm 3\%$ for protons and $\pm 7\%$ for helium. We use these as conservative estimates of the systematic errors in this correction.

4.5.2. *Correction for δ-Electrons*

There is some chance that good events will fail the data cuts because of δ-electrons, which can be produced everywhere in the instrument by the primary particle. The δ-electron production, and consequently the probability that an event will be vetoed, increases with the square of the particle's charge. This is a complicated aspect of the data analysis of any spectrometer, and authors very often just ignore it. For the IMAX spectrum analysis we developed a Monte Carlo program which produces δ-electrons in the various detectors and then follows their tracks through the instrument taking into account the magnetic field configuration of the IMAX spectrometer.

During the ionization process electrons are liberated with energies up to the maximum allowed energy $E_M = 2m_e c^2 \beta^2/1 - \beta^2$. The energy spectrum of these δ-electrons is very steep $[P(E)dE \propto dE/E^2]$, so high-energy δ-electrons are rare, although there are a large number of electrons produced with low energies. For example, a 1 GeV proton ($E_M = 1.2$ MeV) passing through 1 g cm^{-2} of nitrogen liberates around 100 δ-electrons with an energy greater than 1 keV but only ~ 1 electron with an energy greater than 100 keV. The range of an electron with an energy of 1 keV is only a few microns in gas, but at 100 keV the range (around 10 cm) is large enough that the electron could be recognized by the instrument as a secondary particle, leading to a rejection of the event by our preselection and final cuts. Therefore, we have to correct for this effect and calculate how often such a veto occurs.

The energy-dependent angle of emission of the δ-electrons must also be considered since it strongly influences the probability that a δ-electron will separate significantly from the track of the primary particle. The angle of emission of an electron with an energy E is given by the expression $\cos^2 \theta = E/E_M$. This means that for primary particles with low energies, and thus low E_M, the abundant low-energy δ-electrons are emitted close to the forward direction while they are ejected at large angles to the incident track for primary particles with high energies. For high-energy primaries, even δ-electrons with significant energy (and range) are ejected at large angles. For example, a 100 keV δ-electron resulting from the passage of a 1 GeV proton is emitted at 1.3 rad from the primary track.

These basic equations were used in a custom Monte Carlo program with some simplifications. For the multiple Coulomb scattering, we use a Gaussian approximation given in the Review of Particle Properties (Caso et al. 1998). Energy loss is calculated using the Bethe-Bloch formula, which gives a reasonable approximation at the δ-electron energies which are important in this calculation.

Each detector material is divided into small slabs. If a δ-electron of energy E is created in a slab, we propagate the electron through the following slabs of the material taking into account energy loss and multiple scattering. The results of this simulation for the PTFE Cherenkov detector C1 (~ 5 g cm^{-2}) are given in Figure 11, which shows the integral spectra of δ-electrons and the distribution of angles under which these particles emerge from the bottom of C1. The left-hand side represents an incoming proton of 2 GeV and the right-hand side represents a proton of 20 GeV. The 2 GeV protons produce a softer δ-electron spectrum than the 20 GeV protons since only the high-energy protons can produce high-energy δ-electrons ($E_M = 510$ MeV).

The integral flux of δ-electrons above 1 keV emerging from C1 is roughly 40% higher for the incoming protons of 2 GeV than for the 20 GeV protons because the 20 GeV protons cause the abundant low-energy δ-electrons to be emitted at larger angles to the incident track while for the 2 GeV protons they are emitted more in the forward direction. The net effect is that more of the δ-electrons from the 20 GeV protons will stop in the material of C1 and will not reach the bottom. Because of multiple scattering, there is a wide range of angles under which the δ-electrons leave C1. It is clear in Figure 11 that the low-energy δ-electrons are scattered more readily than the high-energy δ-electrons. Similar simulations have been performed for all the other detectors. In the Monte Carlo, the paths of the δ-electrons
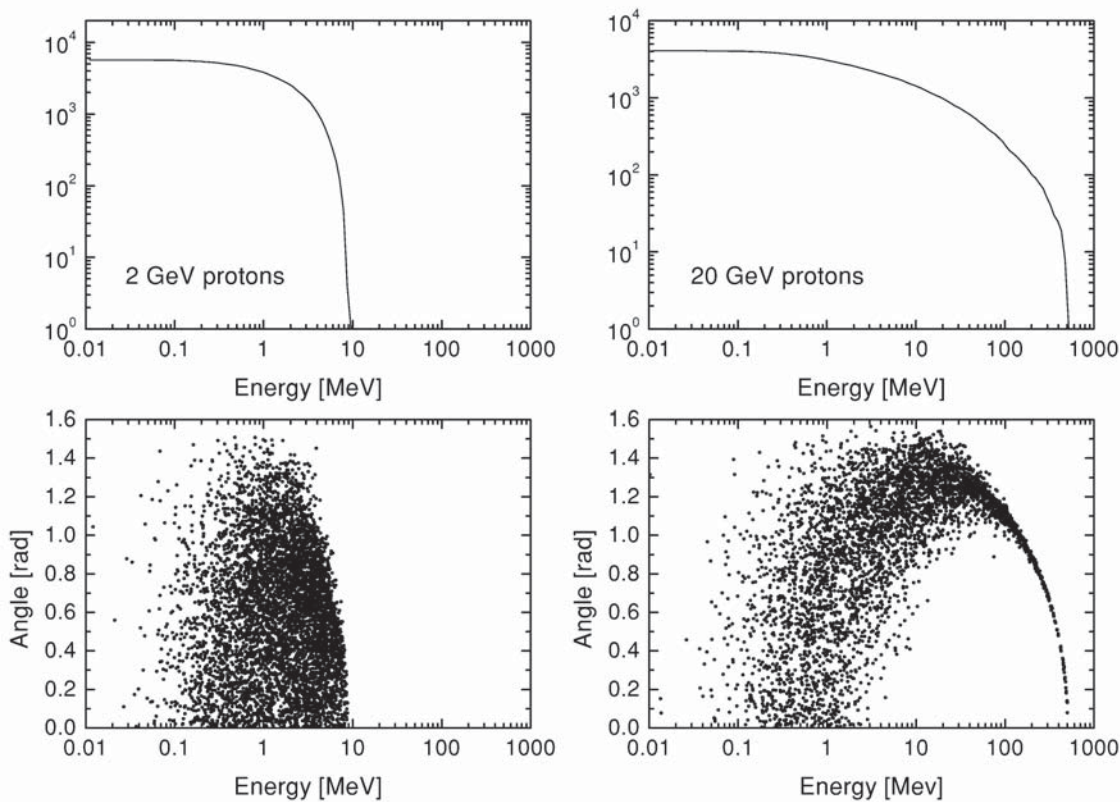
FIG. 11.—Integral spectrum and the emission angle of δ-electrons exiting the bottom of the C1 detector, at left created by 2 GeV protons and at right by 20 GeV protons.

emitted are followed through the instrument in order to find the number of events which will fail the data cuts.

Note that the charge detection efficiency discussed in § 4.4 already includes the effect of δ-electrons. If there is a charge consistency in three scintillators (so that the event passes the preselection), failing the charge cut in the fourth scintillator as a result of the additional charge of a δ-electron is accounted for in the measured efficiency of this detector. Therefore, no additional corrections are necessary.

For the tracking system, a correction must be applied for those events where an accompanying δ-electron would cause the event to fail both the preselection cuts (using the MWPC) *and* the final DC cuts. In order to obtain the percentage of such events using the Monte Carlo, we follow the δ-electrons which emerge from the detectors above the tracking system and solve the equation of motion in the presence of the IMAX magnetic field. Most of the electrons (energies ≤ 10 MeV) spiral around the magnetic field lines. Since our field is inhomogenous, we find that the electrons spiral down toward the magnet, are "reflected," and move upward again. In Figure 12 we show tracks of four different δ-electrons emitted from the S1 scintillator to illustrate the variety of possible electron tracks. As in § 4.4, only those events which would fail both the preselection *and* the final cuts have to be considered, and we find that we have to correct only for a small fraction of the δ-electrons emerging from the detectors above the tracking system.

We also determine the effect of δ-electrons created in the tracking system itself. The grammage of the DC and MWPC is much lower than in the solid scintillators or radiators, so the total number of created δ-electrons is small. However, the emission takes place in the detectors

and the abundant low-energy δ-electrons may travel far enough to generate a multiple track in the tracking devices.

Finally, we check how often a δ-electron will hit a different paddle than the primary particle in the top TOF (δ-electrons emerging from the top of the gondola) or the
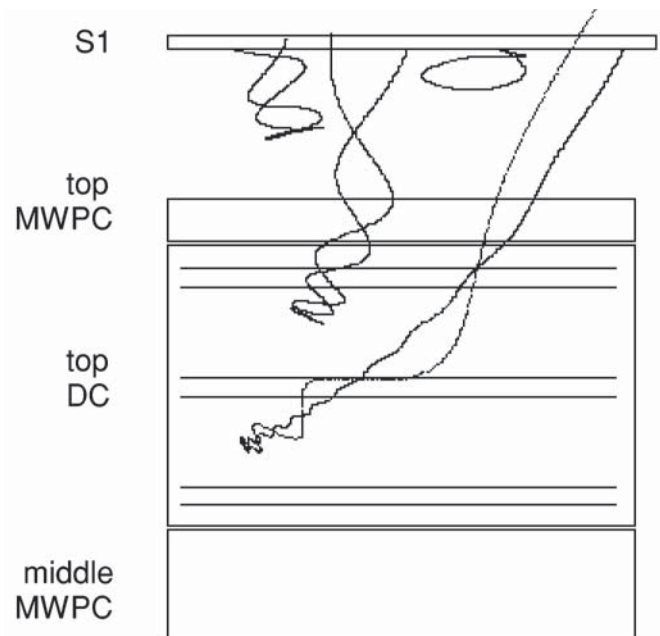

FIG. 12.—Y-coordinate view of tracks of δ-electrons which were created in the S1 detector by 1 GeV protons. This figure demonstrates the variety of possible tracks of δ-electrons.

bottom TOF (δ-electrons created in the detectors above), which would result in a failed "single paddle hit" cut.

The overall correction for δ-electrons is presented in Figure 13. We find that the correction varies between 0.5% and 2.5% (for $Z = 1$ particles), depending on the energy of the primary particle. The largest contribution to the overall correction is due to the δ-electrons which hit a different TOF paddle than the primary particle. The small correction found for IMAX cannot be interpreted as implying that the δ-electron background is small in other experiments since it depends very much on the design of a particular instrument.

4.6. The Absolute Fluxes at the Top of the Instrument

To calculate the absolute flux at the top of the instrument (TOI), the rigidity spectra (particles per GV) measured by the spectrometer are first corrected for background (§ 4.2) and converted to energy. Using the multiplicative correction factors discussed above, the absolute flux is then

$$\text{flux} \left(\frac{\text{particles}}{\text{cm}^2 \text{ s sr GeV nucleon}^{-1}} \right)$$

$$= \text{flux (particles GeV}^{-1} \text{ nucleon}^{-1}) \frac{f_{\text{deconv}}}{t_{\text{eff}} A\Omega\epsilon_{\text{eff}} \epsilon_{\text{int}}}, \quad (6)$$

where f_{deconv} is the "deconvolution factor" (§ 4.3), t_{eff} is the effective flight time, $A\Omega$ is the geometry factor, ϵ_{eff} is the combined detector efficiencies (§ 4.4), and ϵ_{int} is the correction for interactions in the instrument and for δ-electrons (§ 4.5). Background corrections have already been applied.

The effective flight time is derived by multiplying the total flight time by the live-time fraction of the instrument. The live time was measured during the flight by two scalers counting the output of a stable oscillator. One scaler ran without interruption, and the other was inhibited when the instrument was busy. The live-time fraction was found to be 74% $\pm$ 0.01%.

The geometry factor of the instrument is rigidity dependent because the tracks of slow particles are more curved than those for higher rigidities and it is more likely that these slow particles leave the active volumes of the detectors. To calculate this effect, a Monte Carlo simulation was made. For high rigidities the geometry factor was found to be 142 $\pm$ 2 cm^2 sr, decreasing to 100 $\pm$ 2 cm^2 sr at 0.1 GV. This rigidity dependence of the geometry factor is taken into account for the calculation of the fluxes.

The ionization energy loss of the incident particle from the TOI to the spectrometer (a grammage of 10.7 g cm^{-2} to the bottom of the DC) was calculated using routines from Salamon & Ahlen (1981). For each energy bin at the spectrometer, a corresponding energy bin at the TOI was calculated. The TOI spectra were obtained by assigning the (corrected) flux in each of the spectrometer bins to the corresponding TOI bin. Energy loss has a significant effect on the energy bins at low energies. The bins at the TOI are effectively smaller than the bins at the spectrometer, resulting in an enhancement of the flux at TOI.

In addition, ionization energy losses determine the minimum energy a particle must have at the TOA (or top of the atmosphere) to reach the lower TOF and be able to cause a trigger. With a total instrument grammage of 16.7 g cm^{-2} above the lower TOF and 5 g cm^{-2} of atmosphere, this corresponds to an energy of $\sim$170 MeV nucleon^{-1} at the top of atmosphere for protons and ^{4}He and $\sim$200 MeV nucleon^{-1} for ^{3}He. We use these values to define the lower limit of our differential spectra at the TOI. These spectra are given in Tables 2 and 3.

4.7. Corrections for Interactions in the Atmosphere

When cosmic-ray nuclei travel through the atmosphere at balloon flight altitudes their spectra are altered by ionization energy losses (with the largest effects at low energies) and by interactions with the atmospheric gas. For the IMAX flight the residual atmosphere above the instrument was 5 g cm^{-2}. Energy losses in the atmosphere were treated in the same way as in the instrument by calculating the top of the atmosphere (TOA) energy bin corresponding to each TOI bin and rebinning the measured flux accordingly.

The corrections for inelastic interactions are more complex since they lead to a loss of primary particles but also to a gain when particles are produced as secondaries in such interactions. In order to obtain the cosmic-ray spectra for protons and helium at the TOA from measurements with balloon-borne instruments, corrections have to be made for both of these processes. For helium the corrections are relatively simple since the change in the helium flux through the atmosphere is dominated by losses. Secondary production of helium can only occur through spallation of heavier cosmic-ray nuclei, which are rare compared to helium. Thus, the correction factor is simply given by the total nuclear interaction cross section for helium in the atmosphere as given in equation (5). For IMAX this correction leads to an enhancement of the flux at the TOA of about 12%.

For protons the atmospheric correction is more complicated since there is a substantial yield of protons from interactions between all cosmic-ray primaries, including the protons themselves, and air nuclei. Thus, a full correction to the proton spectrum requires a comprehensive atmospheric propagation calculation which includes the various projectiles and the appropriate inclusive production cross sections for secondary protons. For this paper, we adopt the calculation by Papini, Grimani, & Stephens (1996). Essential inputs to such a calculation are the energy spectra of the cosmic radiation at the TOA at different levels of solar activity. For this purpose, the authors derived a set of
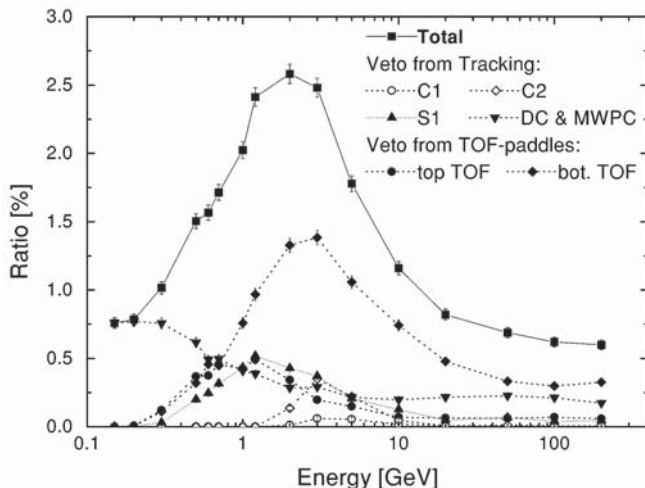

FIG. 13.—Percentage of tracks which fail both the preselection *and* the final cuts for $Z = 1$ particles because of δ-electrons. The solid squares show the overall value.

MENN ET AL.

TABLE 2
THE IMAX PROTON FLUX AT THE TOI AND CORRECTED TO THE TOA

TOP OF INSTRUMENT			TOP OF ATMOSPHERE		
Interval (E_{kin}) (GeV)	Mean (E_{kin}) (GeV)	$F \pm \Delta F_{stat} \pm \Delta F_{syst}$ F(particles $[m^2$ s sr GeV$]^{-1}$)	Interval E_{kin} (GeV)	Mean E_{kin} (GeV)	$F \pm \Delta F_{stat} \pm \Delta F_{syst}$ F(particles $[m^2$ s sr GeV$]^{-1}$)
0.16–0.18......	0.17	$(1.21 \pm 0.02 \pm 0.08) \times 10^3$	0.18–0.20......	0.19	$(6.51 \pm 0.09 \pm 1.35) \times 10^2$
0.18–0.21......	0.20	$(1.14 \pm 0.01 \pm 0.07) \times 10^3$	0.20–0.23......	0.21	$(7.15 \pm 0.08 \pm 1.24) \times 10^2$
0.21–0.25......	0.23	$(1.09 \pm 0.01 \pm 0.07) \times 10^3$	0.23–0.27......	0.25	$(8.01 \pm 0.08 \pm 1.07) \times 10^2$
0.25–0.31......	0.28	$(1.01 \pm 0.01 \pm 0.06) \times 10^3$	0.27–0.33......	0.30	$(8.45 \pm 0.07 \pm 0.83) \times 10^2$
0.31–0.39......	0.35	$(9.71 \pm 0.07 \pm 0.61) \times 10^2$	0.33–0.40......	0.36	$(8.92 \pm 0.06 \pm 0.68) \times 10^2$
0.39–0.49......	0.44	$(8.78 \pm 0.06 \pm 0.55) \times 10^2$	0.40–0.50......	0.45	$(8.48 \pm 0.05 \pm 0.57) \times 10^2$
0.49–0.62......	0.55	$(8.01 \pm 0.05 \pm 0.50) \times 10^2$	0.50–0.63......	0.56	$(7.93 \pm 0.05 \pm 0.51) \times 10^2$
0.62–0.79......	0.70	$(7.13 \pm 0.04 \pm 0.45) \times 10^2$	0.63–0.80......	0.71	$(7.15 \pm 0.04 \pm 0.46) \times 10^2$
0.79–1.01......	0.90	$(6.15 \pm 0.03 \pm 0.38) \times 10^2$	0.80–1.02......	0.91	$(6.22 \pm 0.03 \pm 0.39) \times 10^2$
1.01–1.30......	1.15	$(5.10 \pm 0.03 \pm 0.32) \times 10^2$	1.02–1.31......	1.16	$(5.19 \pm 0.03 \pm 0.33) \times 10^2$
1.30–1.67......	1.47	$(4.16 \pm 0.02 \pm 0.26) \times 10^2$	1.31–1.68......	1.48	$(4.25 \pm 0.02 \pm 0.27) \times 10^2$
1.67–2.14......	1.89	$(3.15 \pm 0.02 \pm 0.20) \times 10^2$	1.68–2.15......	1.90	$(3.24 \pm 0.02 \pm 0.21) \times 10^2$
2.14–2.76......	2.43	$(2.29 \pm 0.01 \pm 0.14) \times 10^2$	2.15–2.77......	2.44	$(2.37 \pm 0.01 \pm 0.15) \times 10^2$
2.76–3.55......	3.13	$(1.56 \pm 0.01 \pm 0.10) \times 10^2$	2.77–3.56......	3.14	$(1.61 \pm 0.01 \pm 0.10) \times 10^2$
3.55–4.58......	4.03	$(1.01 \pm 0.01 \pm 0.06) \times 10^2$	3.56–4.59......	4.04	$(1.05 \pm 0.01 \pm 0.07) \times 10^2$
4.58–5.90......	5.18	$(6.32 \pm 0.05 \pm 0.40) \times 10^1$	4.59–5.91......	5.19	$(6.56 \pm 0.05 \pm 0.42) \times 10^1$
5.90–7.61......	6.68	$(3.85 \pm 0.03 \pm 0.24) \times 10^1$	5.91–7.62......	6.69	$(4.00 \pm 0.03 \pm 0.25) \times 10^1$
7.61–9.81......	8.60	$(2.24 \pm 0.02 \pm 0.14) \times 10^1$	7.62–9.82......	8.61	$(2.33 \pm 0.02 \pm 0.15) \times 10^1$
9.8–12.6	11.1	$(1.24 \pm 0.01 \pm 0.08) \times 10^1$	9.8–12.7	11.1	$(1.29 \pm 0.01 \pm 0.08) \times 10^1$
12.6–16.3......	14.3	$(6.76 \pm 0.08 \pm 0.42) \times 10^0$	12.7–16.3......	14.3	$(7.04 \pm 0.09 \pm 0.44) \times 10^0$
16.3–21.0......	18.4	$(3.63 \pm 0.05 \pm 0.23) \times 10^0$	16.3–21.0......	18.4	$(3.78 \pm 0.06 \pm 0.24) \times 10^0$
21.0–27.1......	23.7	$(2.01 \pm 0.04 \pm 0.13) \times 10^0$	21.0–27.1......	23.8	$(2.10 \pm 0.04 \pm 0.13) \times 10^0$
27.1–35.0......	30.7	$(1.01 \pm 0.02 \pm 0.06) \times 10^0$	27.1–35.0......	30.7	$(1.06 \pm 0.02 \pm 0.07) \times 10^0$
35.0–45.1......	39.5	$(5.12 \pm 0.14 \pm 0.32) \times 10^{-1}$	35.0–45.1......	39.6	$(5.34 \pm 0.15 \pm 0.33) \times 10^{-1}$
45.1–58.2......	50.9	$(2.89 \pm 0.09 \pm 0.18) \times 10^{-1}$	45.1–58.2......	50.9	$(3.01 \pm 0.10 \pm 0.19) \times 10^{-1}$
58.2–75.1......	65.6	$(1.37 \pm 0.56 \pm 0.09) \times 10^{-1}$	58.2–75.1......	65.7	$(1.43 \pm 0.06 \pm 0.09) \times 10^{-1}$
75.1–96.8......	84.8	$(7.18 \pm 0.36 \pm 0.45) \times 10^{-2}$	75.1–96.8......	84.8	$(7.49 \pm 0.37 \pm 0.47) \times 10^{-2}$
97–125	109	$(4.04 \pm 0.23 \pm 0.25) \times 10^{-2}$	97–125	109	$(4.22 \pm 0.24 \pm 0.27) \times 10^{-2}$
125–161	140	$(1.95 \pm 0.14 \pm 0.12) \times 10^{-2}$	125–161	140	$(2.03 \pm 0.15 \pm 0.13) \times 10^{-2}$
161–208	181	$(9.45 \pm 0.05 \pm 0.05) \times 10^{-3}$	161–208	181	$(9.85 \pm 0.88 \pm 0.68) \times 10^{-3}$

simple analytic expressions as best fits to previously observed energy spectra of primary cosmic rays and sorted them into categories of spectra representing maximum (or high) solar activity and minimum (or low) solar activity. For these two categories, they calculate the secondary proton flux and the ratio of secondary protons to remaining primary protons as a function of energy and of atmospheric depth. The correction for secondary protons becomes negligible for energies above ~ 10 GeV, but at lower energies the secondary component contributes considerably to the total measured proton flux (about 5% at 1 GeV); below ~ 200 MeV the secondary protons dominate the proton sample. We can calculate the primary flux at the instrument using this ratio, since the measured proton flux at the instrument is the sum of the remaining primary proton flux and the secondary flux. To correct the primary proton flux at the instrument to the TOA, we calculate the losses in the 5 g cm^{-2} of atmosphere using the total inelastic cross section for protons on nuclei (eq. [4]). We derive a loss of around 5% of the primary protons.

To calculate finally the ratio for the intermediate solar activity level appropriate to the IMAX flight, we use the spherically symmetric force field model of Axford & Gleeson (1968) to describe the solar modulation. First we have to derive values for the terms "minimum" and "maximum" solar activity used by Papini et al. (1996). In the model by Axford & Gleeson (1968) the motion of par-

ticles is described as a diffusion against the solar wind, leading to both convection and energy loss. The average energy loss of particles (mass A, charge Z) from interstellar space to 1 AU is given by the potential energy $\Phi = \phi Z/A$, where ϕ is the solar modulation parameter in MV. The influence of solar modulation on the particle flux is

$$J_{mod}(E) = \frac{E^2 + 2m_p c^2 E}{(E + \Phi)^2 + 2m_p c^2 (E + \Phi)} J(E + \Phi) , \quad (7)$$

where E is the kinetic energy in MeV per nucleon, m_p is the mass of a proton, and $J(E)$ is the interstellar flux. We found that the two spectra used by Papini et al. (1996) are best described with $\phi = 500$ MV for "minimum" and $\phi = 1000$ MV for "maximum" solar activity. To get the appropriate value for ϕ at the time of the IMAX flight, we used published values of ϕ from other balloon experiments (Seo et al. 1992; Beatty et al. 1993; Salamon et al. 1990; Webber et al. 1991) and results from Labrador & Mewaldt (1997) together with the corresponding neutron monitor counts. We estimate a modulation parameter for the IMAX flight of 750 ± 50 MV. Since we do not exactly know how this modulation parameter influences the secondary-to-primary ratio, we perform a linear interpolation between the two boundary values as a function of energy. As a result, the IMAX secondary-to-primary proton ratio is right in the middle between the limits given by the minimum and

TABLE 3

THE IMAX HELIUM FLUX AT THE TOI AND CORRECTED TO THE TOA

TOP OF INSTRUMENT			TOP OF ATMOSPHERE		
Interval E_{kin} (GeV nucleon^{-1})	Mean E_{kin} (GeV nucleon^{-1})	$F \pm \Delta F_{stat} \pm \Delta F_{syst}$ F(particles [m^2 s sr GeV nucleon^{-1}]$^{-1}$)	Interval E_{kin} (GeV nucleon^{-1})	Mean E_{kin} (GeV nucleon^{-1})	$F \pm \Delta F_{stat} \pm \Delta F_{syst}$ F(particles [m^2 s sr GeV nucleon^{-1}]$^{-1}$)
0.21–0.25	0.23	$(1.43 \pm 0.05 \pm 0.13) \times 10^2$	0.23–0.27	0.25	$(1.65 \pm 0.06 \pm 0.15) \times 10^2$
0.25–0.31	0.28	$(1.55 \pm 0.04 \pm 0.14) \times 10^2$	0.27–0.33	0.30	$(1.77 \pm 0.05 \pm 0.16) \times 10^2$
0.31–0.39	0.35	$(1.48 \pm 0.03 \pm 0.13) \times 10^2$	0.33–0.40	0.36	$(1.67 \pm 0.04 \pm 0.15) \times 10^2$
0.39–.49	0.44	$(1.40 \pm 0.03 \pm 0.12) \times 10^2$	0.40–0.50	0.45	$(1.58 \pm 0.03 \pm 0.14) \times 10^2$
0.49–0.62	0.55	$(1.23 \pm 0.02 \pm 0.11) \times 10^2$	0.50–0.63	0.56	$(1.38 \pm 0.02 \pm 0.12) \times 10^2$
0.62–0.79	0.70	$(9.94 \pm 0.17 \pm 0.88) \times 10^1$	0.63–0.80	0.71	$(1.12 \pm 0.02 \pm 0.10) \times 10^2$
0.79–1.01	0.89	$(8.13 \pm 0.14 \pm 0.72) \times 10^1$	0.80–1.02	0.90	$(9.12 \pm 0.15 \pm 0.81) \times 10^1$
1.01–1.30	1.15	$(6.37 \pm 0.11 \pm 0.57) \times 10^1$	1.02–1.31	1.16	$(7.15 \pm 0.12 \pm 0.64) \times 10^1$
1.30–1.67	1.47	$(4.56 \pm 0.08 \pm 0.41) \times 10^1$	1.31–1.68	1.48	$(5.12 \pm 0.09 \pm 0.46) \times 10^1$
1.67–2.14	1.89	$(3.09 \pm 0.06 \pm 0.28) \times 10^1$	1.68–2.15	1.90	$(3.47 \pm 0.07 \pm 0.31) \times 10^1$
2.14–2.76	2.43	$(1.99 \pm 0.04 \pm 0.18) \times 10^1$	2.15–2.77	2.44	$(2.23 \pm 0.05 \pm 0.20) \times 10^1$
2.76–3.55	3.12	$(1.20 \pm 0.03 \pm 0.11) \times 10^1$	2.77–3.56	3.13	$(1.34 \pm 0.03 \pm 0.12) \times 10^1$
3.55–4.58	4.03	$(7.00 \pm 0.19 \pm 0.62) \times 10^0$	3.56–4.59	4.04	$(7.84 \pm 0.21 \pm 0.70) \times 10^0$
4.58–5.90	5.18	$(3.89 \pm 0.12 \pm 0.35) \times 10^0$	4.59–5.91	5.19	$(4.36 \pm 0.14 \pm 0.39) \times 10^0$
5.90–7.61	6.66	$(2.19 \pm 0.08 \pm 0.19) \times 10^0$	5.91–7.62	6.67	$(2.46 \pm 0.09 \pm 0.22) \times 10^0$
7.61–9.81	8.61	$(1.35 \pm 0.06 \pm 0.12) \times 10^0$	7.62–9.82	8.62	$(1.51 \pm 0.06 \pm 0.14) \times 10^0$
9.8–12.6	11.1	$(6.51 \pm 0.35 \pm 0.58) \times 10^{-1}$	9.8–12.7	11.1	$(7.30 \pm 0.39 \pm 0.65) \times 10^{-1}$
12.6–16.3	14.3	$(3.29 \pm 0.22 \pm 0.29) \times 10^{-1}$	12.7–16.3	14.3	$(3.68 \pm 0.25 \pm 0.33) \times 10^{-1}$
16.3–21.0	18.6	$(2.18 \pm 0.16 \pm 0.19) \times 10^{-1}$	16.3–21.0	18.6	$(2.44 \pm 0.18 \pm 0.22) \times 10^{-1}$
21.0–27.1	23.8	$(1.02 \pm 0.10 \pm 0.09) \times 10^{-1}$	21.0–27.1	23.8	$(1.15 \pm 0.11 \pm 0.10) \times 10^{-1}$
27.1–35.0	30.4	$(5.95 \pm 0.66 \pm 0.53) \times 10^{-2}$	27.1–35.0	30.4	$(6.66 \pm 0.74 \pm 0.60) \times 10^{-2}$
35.0–45.1	39.2	$(2.47 \pm 0.38 \pm 0.22) \times 10^{-2}$	35.0–45.1	39.2	$(2.76 \pm 0.42 \pm 0.25) \times 10^{-2}$
45.1–58.2	50.9	$(1.18 \pm 0.23 \pm 0.11) \times 10^{-2}$	45.1–58.2	50.9	$(1.32 \pm 0.26 \pm 0.12) \times 10^{-2}$
58.2–75.1	65.5	$(6.86 \pm 1.50 \pm 0.69) \times 10^{-3}$	58.2–75.1	65.5	$(7.69 \pm 1.68 \pm 0.78) \times 10^{-3}$
75.1–96.8	84.6	$(2.37 \pm 0.75 \pm 0.30) \times 10^{-3}$	75.1–96.8	84.6	$(2.66 \pm 0.84 \pm 0.33) \times 10^{-3}$
97–125	108	$(1.85 \pm 0.56 \pm 0.30) \times 10^{-3}$	97–125	108	$(2.07 \pm 0.62 \pm 0.34) \times 10^{-3}$

maximum solar modulation. We use these limits to set a conservative error of the ratio. At low energies this error is large (about 30% at 200 MeV) and will dominate the total systematic error of the proton spectrum.

5. RESULTS

The measured IMAX fluxes extrapolated to the TOA are given in Tables 2 and 3 along with the TOI fluxes. We show separate columns for the statistical and systematic errors. The mean kinetic energy listed in Tables 2 and 3 are determined from the arithmetic mean of the measured rigidities for each energy bin and so reflect the spectral weighting toward lower energy. The TOA spectra are shown in Figure 14. In this figure the total uncertainty is smaller than the plot symbols except at the lowest proton energy and the highest helium energies. The total uncertainty in each point is indicated by the vertical bar and the statistical uncertainty by the cross bars.

The spectra can be represented by $(8.03 \pm 1.36) \times 10^3 E^{-2.61 \pm 0.04}$ (m^2 GeV s sr)$^{-1}$ for protons between 20 and 200 GeV and $(4.33 \pm 1.05) \times 10^2 E^{-2.63 \pm 0.08}$ (m^2 GeV nucleon^{-1} s sr)$^{-1}$ for helium nuclei between 10 and 100 GeV nucleon^{-1}. With IMAX, we could not observe the effect of geomagnetic cutoff on the low-energy part of the spectrum since the energies which are necessary to penetrate the instrument are relatively high (§ 4.6). The cutoff values presented in § 3 correspond to a kinetic cutoff energy of 70 MeV for protons and 18 MeV nucleon^{-1} for ^{4}He at Lynn Lake and 191 MeV for protons and 52 MeV nucleon^{-1} for ^{4}He at the landing site Peace River. These

values are generally smaller then the instrumental cutoff, particularly if ionization energy losses in the atmosphere are considered.

In Figure 15, we show the IMAX spectra at the TOA compared with results from Smith et al. (1973), Seo et al. (1992), Webber et al. (1987), Bellotti et al. (1999; MASS2 experiment), and Boezio et al. (1999; CAPRICE experiment). While Smith et al. (1973) used a superconducting magnet and spark chambers as a spectrometer (MDR ~ 50 GV), the measurements of Seo et al. (1992) and
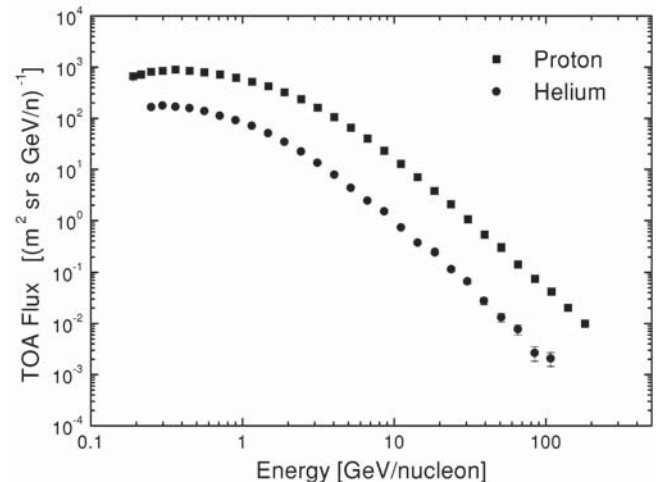

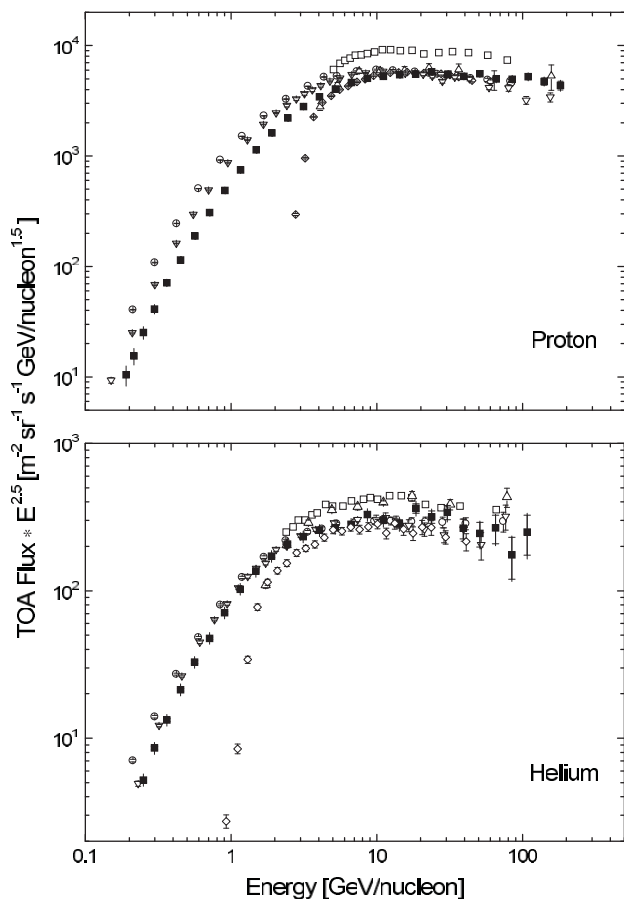FIG. 14.—IMAX differential energy spectra at the TOA for protons and helium.

FIG. 15.—IMAX fluxes compared to other balloon measurements. *Filled squares:* Our results. *Inverted triangles:* Boezio et al. (1999). *Diamonds:* Bellotti et al. (1999). *Circles:* Seo et al. (1992). *Open squares:* Webber et al. (1987). *Upright triangles:* Smith et al. (1973). The treatment of systematic error varies among these measurements. This should be considered when comparing them.

Webber et al. (1987) were performed using the same magnet as IMAX but with only MWPCs for tracking, resulting in an MDR of about 50–100 GV. However, the MASS2 experiment, flown in 1991 near solar maximum, used similar drift chambers and the same MWPCs as IMAX (reaching an MDR of 210 GV for protons). The CAPRICE experiment, flown in 1994 near solar minimum, employed the same spectrometer as IMAX (reaching an MDR of 172 GV for protons). Both experiments used different ancillary detectors. For high-energy protons there is generally good agreement between the earlier measurements of Smith et al. (1973) and Seo et al. (1992) and the present results, while the measurements of Webber et al. (1987) are consistently higher. For helium, the high-energy results generally agree within uncertainties, although the Webber et al. (1987) results are somewhat high. The MASS2 and CAPRICE results are in good agreement with the IMAX points around 10 GeV with a slightly steeper spectrum at higher energies. Note that the MASS2 and CAPRICE spectra are not deconvolved at high energies, so the differences would be smaller if this correction were applied. At low energies it is difficult to compare the various measurements due to the influence of solar modulation or geomagnetic cutoff. (The geomagnetic cutoff for the MASS2 experiment was about 4.5 GV.)

To derive interstellar spectra, the TOA spectra shown in Figure 14 must be adjusted for the effect of solar modulation. Even at 20 GeV the suppression of the proton flux for a solar modulation parameter of $\phi = 750$ MV is still on the order of 5% (using the force field model). If we fit the high-energy part of the spectrum between 20 GeV and 100 GeV using a power law and ignore this effect, the derived spectral index would be decreased by about 0.05. Therefore, to obtain interstellar spectra, the IMAX energy spectra were first demodulated using a force field approximation with a modulation parameter of $\phi = 750$ MV for both protons and helium and then converted to rigidity spectra. These are presented in Figure 16. Both the proton and helium spectra are consistent with a pure power law in rigidity, although the helium spectrum shows minor differences at lower rigidities. The deviation of the helium spectrum from a pure power law can be reduced by using a higher value of the solar modulation parameter, suggesting that a slightly different modulation parameter should be used for protons and helium if the force field approximation is employed. If a power law is fitted to the data between 20 and 200 GV, the derived interstellar spectra are well described by $(1.42 \pm 0.21) \times 10^4 R^{2.71 \pm 0.04}$ (m^2 GV s sr)$^{-1}$ for protons and $(3.15 \pm 1.03) \times 10^3 R^{2.79 \pm 0.08}$ (m^2 GV s sr)$^{-1}$ for helium. The p/He ratio at the TOA as a function of rigidity between 5 and 100 GV is found to be nearly constant at 5.9 ± 0.7.

It is interesting to consider how well the extrapolated IMAX spectra agree with measurements made at higher energies. In Figure 17 we show the IMAX interstellar rigidity spectra in comparison with measurements performed by high-energy balloon-borne and satellite experiments (Asakimori et al. 1998 [JACEE]; Zatsepin et al. 1993 [MUBEE]; Ivanenko et al. 1993 [SOKOL]; Ichimura et al. 1993; Buckley et al. 1994 [RICH]; Ryan, Ormes, & Balasubramanyan 1972). Also shown are the bands for a 95% confidence level of the fit to the IMAX proton and helium data between 20 and 200 GV. Where no flux tables were published, the data presented in this figure were derived from the papers by measuring the published plots and then converting to rigidity spectra. For rigidities greater than 1
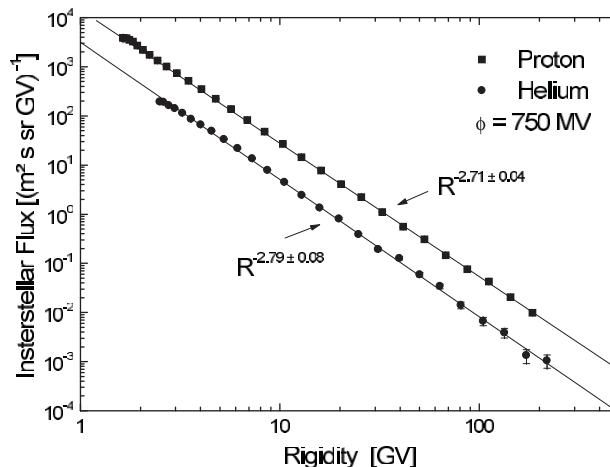

FIG. 16.—IMAX interstellar rigidity spectra, demodulated with the force field formula and a modulation parameter of $\phi = 750$ MV. Both spectra are in good agreement with pure power laws in rigidity.
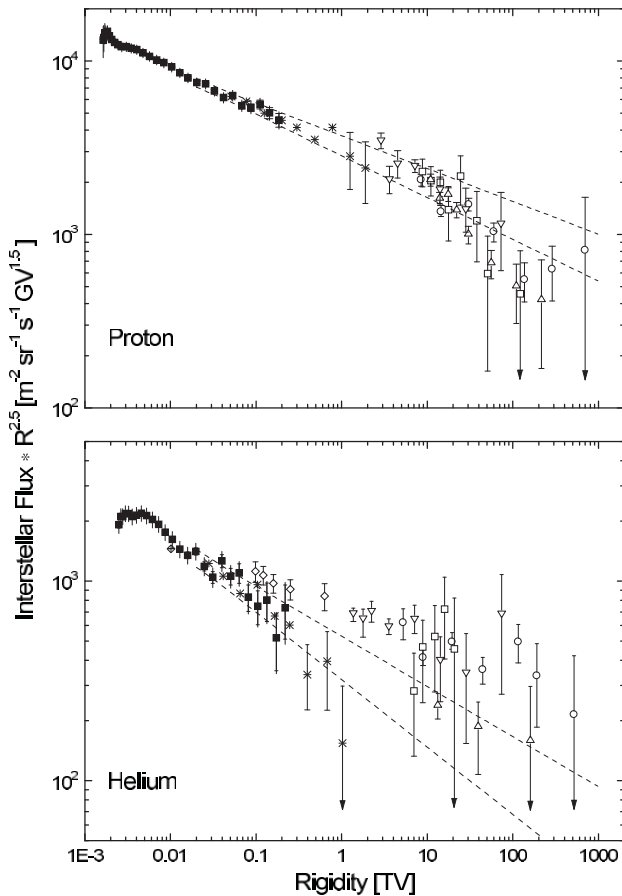
FIG. 17.—IMAX fluxes compared to the high-energy measurements made with balloon- and satellite-borne emulsion chambers and calorimeters. *Filled squares:* Our results. *Circles:* Asakimori et al. (1998). *Diamonds:* Buckley et al. (1994). *Open squares:* Ichimura et al. (1993). *Inverted triangles:* Ivanenko et al. (1993). *Upright triangles:* Zatsepin et al. (1993). *Asterisks:* Ryan et al. (1972). The dotted lines are the bands for a 95% confidence level of the fit to the IMAX proton and helium data between 20 and 200 GV.

statistical errors at high rigidities. The extrapolation of the proton spectrum measured by IMAX is in good agreement with the results measured by other instruments up to about 10 TV, but for higher rigidities the measured spectrum appears to become steeper. For helium the spectrum as measured by SOKOL (Ivanenko et al. 1993) and JACEE (Asakimori et al. 1998) is considerably flatter than the extrapolation of the IMAX helium spectrum. This would suggest a transition in the shape of the helium spectrum in the low-TeV regime.

6. CONCLUSIONS

The IMAX collaboration has measured the cosmic-ray proton and helium spectra from 0.2 GeV nucleon^{-1} to about 200 GeV nucleon^{-1}. The quality of the magnetic spectrometer was superior to those used in earlier measurements, achieving an MDR of ~ 180 GV for protons and ~ 250 GV for helium. The rich instrumentation of the experiment allowed an extensive examination of the instrument efficiency to be carried out using redundant detectors. In this way we reduced the bias in the efficiency.

The interstellar spectra derived from the IMAX measurements can be represented by power laws in rigidity if demodulated with a solar modulation parameter of $\phi = 750$ MV. The resulting spectral indices are 2.71 ± 0.04 for protons and 2.79 ± 0.08 for helium. The IMAX measurements have significantly improved the accuracy with which the absolute fluxes of the most abundant particles in the primary cosmic radiation are known. The absolute fluxes of protons and helium are determined by IMAX to a precision of 20% compared to the dispersion among earlier measurements of about a factor of 2.

TV, the general trend seems to be that the helium spectrum measured in these experiments is flatter than the proton spectrum. At around 1000 TV the fluxes are equal, although it is difficult to draw firm conclusions because of the large

APPENDIX A

THE HELIUM ISOTOPE SPECTRA

As mentioned in § 4.1, we derived the helium energy spectrum from the raw rigidity spectrum by taking all $Z = 2$ particles as ^{4}He as in previous papers. This results in an error, since there is a nonnegligible abundance of ^{3}He and the conversion from rigidity to energy will be incorrect for this component if it is treated as ^{4}He. Reimer et al. (1998) presented the ^{3}He/^{4}He ratio measured with IMAX between 0.2 and 3.7 GeV nucleon^{-1} at the spectrometer and a detailed description of the propagation code used to derive the corresponding ratio at the TOA. This code was used to calculate a best-fit curve to the measured ratio at the spectrometer. The ratio at higher energies depends mostly on assumptions concerning the path length distribution for cosmic rays in the galaxy. Details can be found in Reimer et al. (1998).

We used this best-fit curve as a constraint, requiring our final ^{3}He and ^{4}He spectra to be consistent with this ratio at the instrument. We first determine the ^{3}He/^{4}He ratio as a function of rigidity in a similar way to the procedure for ^{1}H and ^{2}H described in § 4.2. We start with the measured helium rigidity spectrum at the spectrometer. With a rigidity dependent ^{3}He/^{4}He ratio as a free parameter, we calculate independent rigidity spectra for ^{3}He and ^{4}He. Multiplying by the appropriate values for the detector efficiencies, deconvolution factor, etc., we calculate the ^{3}He and ^{4}He flux and finally convert the rigidity

spectra to energy spectra. We use the ^{3}He and ^{4}He energy spectra to derive the ^{3}He/^{4}He ratio at the spectrometer. (Appropriate rigidity bins for ^{3}He and ^{4}He must be used to give equal bins in energy.) Comparing this ratio to the best-fit curve derived earlier, we calculate a χ^2. The rigidity dependent ratio is then found by minimizing χ^2.

In this way we directly determine the ^{3}He and ^{4}He spectra at the spectrometer. The propagation of these spectra to the TOA is different from § 4.7, where we just took the losses of ^{4}He in the atmosphere and the instrument into account and derived energy-dependent loss factors. Now we have to use the propagation code since we have still losses but also an enhanced flux of ^{3}He at the spectrometer due to the spallation of ^{4}He. Using this code we calculate the fluxes of ^{3}He and ^{4}He at the TOA, given in Table 4. In Figure 18 we present the two spectra. The total helium flux can be derived by adding the ^{3}He and ^{4}He flux. (To get equal energy bins at the TOA, we used a different energy binning for ^{3}He and ^{4}He at the spectrometer, which were then corrected for the energy loss to the TOA.) Thus, we derive two results for the total helium flux at the TOA, the result of the "standard" approach where all helium is taken as ^{4}He (§ 5), and the result of our improved calculation where

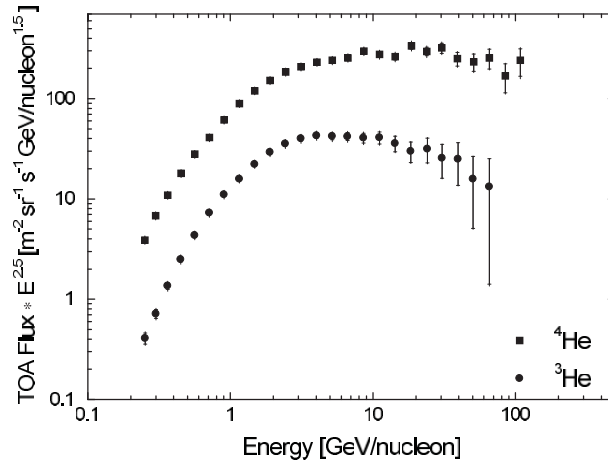Fig. 18.—Differential ^{3}He and ^{4}He spectra extrapolated to the TOA. The two spectra are calculated from the total spectrum of helium nuclei using the ^{3}He/^{4}He ratio measured by IMAX between 0.2 and 3.7 GeV nucleon^{-1} and a model of Galactic propagation (Reimer et al. 1998).

TABLE 4

THE IMAX HELIUM ISOTOPE FLUX CORRECTED TO THE TOA

Interval E_{kin} (GeV nucleon^{-1})	Mean E_{kin} (GeV nucleon^{-1})	^{3}He Flux $(F \pm \Delta F_{stat} \pm \Delta F_{syst})$ (particles [m^2 s sr GeV nucleon^{-1}]$^{-1}$)	^{4}He Flux $(F \pm \Delta F_{stat} \pm \Delta F_{syst})$ (particles [m^2 s sr GeV nucleon^{-1}]$^{-1}$)
0.23–0.25	0.25	$(1.27 \pm 0.16 \pm 0.11) \times 10^1$	$(1.23 \pm 0.05 \pm 0.11) \times 10^2$
0.27–0.31	0.30	$(1.44 \pm 0.15 \pm 0.13) \times 10^1$	$(1.40 \pm 0.04 \pm 0.12) \times 10^2$
0.33–0.39	0.36	$(1.70 \pm 0.13 \pm 0.15) \times 10^1$	$(1.37 \pm 0.04 \pm 0.12) \times 10^2$
0.4–0.49	0.45	$(1.85 \pm 0.11 \pm 0.16) \times 10^1$	$(1.33 \pm 0.03 \pm 0.12) \times 10^2$
0.50–0.62	0.56	$(1.84 \pm 0.09 \pm 0.16) \times 10^1$	$(1.17 \pm 0.02 \pm 0.10) \times 10^2$
0.63–0.79	0.71	$(1.70 \pm 0.08 \pm 0.15) \times 10^1$	$(9.60 \pm 0.18 \pm 0.85) \times 10^1$
0.80–1.01	0.90	$(1.42 \pm 0.06 \pm 0.13) \times 10^1$	$(7.91 \pm 0.15 \pm 0.70) \times 10^1$
1.02–1.30	1.16	$(1.11 \pm 0.05 \pm 0.10) \times 10^1$	$(6.25 \pm 0.11 \pm 0.56) \times 10^1$
1.31–1.67	1.48	$(8.36 \pm 0.35 \pm 0.74) \times 10^0$	$(4.51 \pm 0.09 \pm 0.40) \times 10^1$
1.68–2.14	1.90	$(5.95 \pm 0.26 \pm 0.53) \times 10^0$	$(3.07 \pm 0.06 \pm 0.27) \times 10^1$
2.15–2.76	2.44	$(3.86 \pm 0.19 \pm 0.34) \times 10^0$	$(1.99 \pm 0.04 \pm 0.18) \times 10^1$
2.77–3.55	3.13	$(2.32 \pm 0.13 \pm 0.21) \times 10^0$	$(1.20 \pm 0.03 \pm 0.11) \times 10^1$
3.56–4.58	4.04	$(1.32 \pm 0.08 \pm 0.12) \times 10^0$	$(7.04 \pm 0.20 \pm 0.63) \times 10^0$
4.59–5.90	5.19	$(6.89 \pm 0.52 \pm 0.61) \times 10^{-1}$	$(3.93 \pm 0.13 \pm 0.35) \times 10^0$
5.91–7.61	6.67	$(3.68 \pm 0.33 \pm 0.33) \times 10^{-1}$	$(2.22 \pm 0.09 \pm 0.20) \times 10^0$
7.62–9.81	8.62	$(1.87 \pm 0.21 \pm 0.17) \times 10^{-1}$	$(1.37 \pm 0.06 \pm 0.12) \times 10^0$
9.8–12.6	11.1	$(9.95 \pm 1.36 \pm 0.89) \times 10^{-2}$	$(6.69 \pm 0.38 \pm 0.59) \times 10^{-1}$
12.7–16.3	14.3	$(4.66 \pm 0.82 \pm 0.41) \times 10^{-2}$	$(3.39 \pm 0.24 \pm 0.30) \times 10^{-1}$
16.3–21.0	18.6	$(2.06 \pm 0.48 \pm 0.18) \times 10^{-2}$	$(2.27 \pm 0.17 \pm 0.20) \times 10^{-1}$
21.0–27.1	23.8	$(1.12 \pm 0.31 \pm 0.10) \times 10^{-2}$	$(1.07 \pm 0.11 \pm 0.10) \times 10^{-1}$
27.1–35.0	30.4	$(4.96 \pm 1.83 \pm 0.45) \times 10^{-3}$	$(6.27 \pm 0.72 \pm 0.56) \times 10^{-2}$
35.0–45.1	39.2	$(2.55 \pm 1.16 \pm 0.22) \times 10^{-3}$	$(2.61 \pm 0.41 \pm 0.23) \times 10^{-2}$
45.1–58.2	50.9	$(8.78 \pm 5.96 \pm 0.78) \times 10^{-4}$	$(1.26 \pm 0.25 \pm 0.12) \times 10^{-2}$
58.2–75.1	65.5	$(3.81 \pm 3.40 \pm 0.35) \times 10^{-4}$	$(7.35 \pm 1.63 \pm 0.74) \times 10^{-3}$
75.1–96.8	84.6	...	$(2.56 \pm 0.82 \pm 0.31) \times 10^{-3}$
97–125	108	...	$(2.00 \pm 0.61 \pm 0.32) \times 10^{-3}$

we take the measured ^{3}He/^{4}He ratio into account. Calculating the ratio of these two spectra we find that the standard approach overestimates the total helium flux at low energies by about 20% at 250 MeV nucleon^{-1}, while it is about 6% lower at around 4 GeV nucleon^{-1}. With increasing energy the difference becomes smaller yet.

REFERENCES

Aksinenko, V. D., et al. 1980, Nucl. Phys. A, 348, 518
Asakimori, K., et al. 1998, ApJ, 502, 278
Auce, A., et al. 1994, Phys. Rev. C, 50, 871
Axford, W. I., & Gleeson, L. J. 1968, ApJ, 154, 1011
Beatty, J. J., et al. 1993, ApJ, 413, 268
Bellotti, R., et al. 1999, Phys. Rev. D, 60, 052002
Boezio, M., et al. 1999, ApJ, 518, 457
Buckley, J., et al. 1994, ApJ, 429, 736
Caso, C., et al. 1998, European Phys. J., C3, 1
DeVries, R. M., et al. 1982, Phys. Rev. C, 26, 301
Dubar, L. V., et al. 1989, Soviet J. Nucl. Phys., 49(5), 771
Gaisser, T. K. 1990, Cosmic Rays and Particle Physics (Cambridge: Cambridge Univ. Press)
Gaisser, T. K., & Schaefer, R. K. 1992, ApJ, 394, 174
Gluckstern, R. L. 1963, Nucl. Instrum. Methods, 24, 381
Golden, R. L., et al. 1978, Nucl. Instrum. Methods, 148, 179
———. 1991, Nucl. Instrum. Methods, A306, 366
Hof, M., et al. 1994, Nucl. Instrum. Methods, A345, 561
Ichimura, M., et al. 1993, Phys. Rev. D, 48(5), 1949
Ivanenko, I. P., et al. 1993, Proc. 23d Int. Cosmic-Ray Conf. (Calgary), 2, 17
Labrador, A. W., & Mewaldt, R. A. 1997, ApJ, 480, 371
Letaw, J. R., Silberberg, R., & Tsao, C. H. 1983, ApJS, 51, 271
Mitchell, J. W., et al. 1993a, Proc. 23d Int. Cosmic-Ray Conf. (Calgary), 1, 519

Mitchell, J. W., et al. 1993b, Proc. 23d Int. Cosmic-Ray Conf. (Calgary), 2, 627
———. 1996, Phys. Rev. Lett., 76, 3057
Papini, P., Grimani, C., & Stephens, S. A. 1996, Nuovo Cimento, 19, 367
Reimer, O., et al. 1995, Proc. 24th Int. Cosmic-Ray Conf. (Rome), 2, 614
———. 1998, ApJ, 496, 490
Ryan, M. J., Ormes, J. F., & Balasubrahmanyan, V. K. 1972, Phys. Rev. Lett., 28, 985
Salamon, M. H., & Ahlen, S. P. 1981, Phys. Rev. B, 24, 5026
Salamon, M. H., et al. 1990, ApJ, 349, 78
Seo, E. S., et al. 1992, Nucl. Tracks Radiat. Meas., 20(3), 431
Shea, M. A., & Smart, D. F. 1983, Proc. 18th Int. Cosmic Ray Conf. (Bangalore), 3, 415
Smith, L. H., et al. 1973, ApJ, 180, 987
Tanihata, I., et al. 1985, Phys. Lett. 160B, 380
Webber, W. R., et al. 1987, Proc. 20th Int. Cosmic Ray Conf. (Moscow), 1, 325
———. 1990a, Phys. Rev. C, 41, 520
———. 1990b, Phys. Rev. C, 41, 533
———. 1990c, Phys. Rev. C, 41, 547
———. 1990d, Phys. Rev. C, 41, 566
———. 1991, ApJ, 380, 230
Zatsepin, V. I., et al. 1993, Proc. 23d Int. Cosmic-Ray Conf. (Calgary), 2, 13